Article

AhR inhibition promotes axon regeneration via a stress–growth switch

https://doi.org/10.1038/s41586-026-10295-z

Received: 13 September 2023

Accepted: 18 February 2026

Published online: 01 April 2026

Open access

Check for updates

Dalia Halawani[1,5,7], Yiqun Wang[1,6,7], Jiaxi Li[1], Daniel Halperin[1], Haofei Ni[1], Molly Estill[1], Aarthi Ramakrishnan[1], Li Shen[1], Arthur Sefiani[2], Cédric G. Geoffroy[2,3], Roland H. Friedel[1,4] & Hongyan Zou[1,4]✉

Axon regeneration is limited in the mammalian central nervous system[1]. Neurons must balance stress responses with regenerative demands after axonal injury[2], but the mechanisms remain unclear. Here we identify aryl hydrocarbon receptor (AhR), a ligand-activated basic helix–loop–helix/PER-ARNT-SIM (bHLH-PAS) transcription factor, as a key regulator of this stress–growth switch. We show that ligand-mediated AhR signalling restrains axon growth, whereas neuronal deletion or pharmacological inhibition of AhR promotes axonal regeneration and functional recovery in both peripheral nerve and spinal cord injury models. Mechanistic studies reveal that axotomy-induced AhR activation in dorsal root ganglion neurons enforces proteostasis and stress-response programs to preserve tissue integrity. By contrast, AhR ablation redirects the neuronal response towards elevated de novo translation and pro-growth signalling, enabling axon regeneration. This growth-promoting effect requires HIF1α, with shared transcriptional targets enriched for metabolic and regenerative pathways. Single-cell and epigenomic analyses further revealed that the AhR regulon engages the integrated stress response and DNA hydroxymethylation to rewire neuronal injury-response programs. Together, our findings establish AhR as a neuronal brake on axon regeneration, integrating environmental sensing, protein homeostasis and metabolic signalling to control the balance between stress adaptation and axonal repair.

Neural injury disrupts the extracellular milieu through tissue breakdown, neuroinflammation and altered oxygen tension. To cope with stress, injured neurons deploy safeguard mechanisms that adjust metabolism, synaptic activity and regenerative gene programs. However, how neurons coordinate the balance between stress adaptation and regenerative demands remains poorly understood.

Basic helix–loop–helix/PER-ARNT-SIM (bHLH-PAS) transcription factors (TFs) act as molecular sensors of environmental and physiological signals. Within this family, BMAL1 coordinates circadian rhythm, HIF1α mediates hypoxia responses and AhR detects xenobiotics and endogenous metabolites[3,4]. We recently showed that BMAL1 gates regenerative responses of dorsal root ganglion (DRG) neurons after peripheral axotomy[5] and others showed that intermittent hypoxia enhances axon regeneration through HIF1α activation[6]. AhR and HIF1α are structurally related α-subunits that share the dimerization partner ARNT (HIF1β), yet the roles of AhR or ARNT in axonal injury, and their interplay with HIF1α and BMAL1, remain largely unexplored.

AhR is unique among bHLH-PAS TFs as the only ligand-activated member[7]. Originally identified as a sensor of environmental toxins such as dioxin, AhR responds to diverse dietary, microbial and metabolic molecules[7]. After ligand binding, AhR translocates to the nucleus, dimerizes with ARNT and regulates transcription through AhR response elements (AHREs)[8]. Canonical AhR signalling induces xenobiotic-metabolizing enzymes of the P450 family and NRF2-dependent antioxidants. Multiple feedback mechanisms restrain AhR activity, including CYP1-mediated ligand metabolism[9] and induction of the AhR repressor (AhRR), underscoring the need for tight control to prevent toxicity from sustained AhR activation[8].

Competition with HIF1α for ARNT provides an additional regulatory layer[10]. Depending on the temporal and cellular context, AhR and HIF1α can antagonize, cooperate or synergize[11,12]. Recent work suggests temporally gated access to ARNT, with HIF1α acting first and AhR subsequently taking over[12].

Although AhR has been extensively studied in toxicology, barrier tissue biology and immunity, its neuronal functions, particularly in injury, remain poorly defined. DRG neurons offer an excellent model for axon regeneration: peripheral axotomy elicits robust regrowth, whereas central axotomy does not; however, a conditioning peripheral nerve lesion (PL) can prime central DRG axons for regeneration[13,14].

Here we show that DRG neurons are responsive to ligand-mediated AhR signalling, which acts as a brake on axon regeneration. Neuronal deletion of AhR enhanced axonal regrowth in both peripheral nerve

[1]Nash Family Department of Neuroscience, Friedman Brain Institute, Icahn School of Medicine at Mount Sinai, New York, NY, USA. [2]Department of Neuroscience and Experimental Therapeutics, College of Medicine, Texas A&M University, College Station, TX, USA. [3]Wolfson Sensory, Pain and Regeneration Centre (SPaRC), King's College London, London, UK. [4]Department of Neurosurgery, Icahn School of Medicine at Mount Sinai, New York, NY, USA. [5]Present address: Center for Pharmacology, Institute II, Faculty of Medicine, University Hospital Cologne, Cologne, Germany. [6]Present address: Sports Medicine Center, Honghui Hospital, Xi'an Jiaotong University, Xi'an, China. [7]These authors contributed equally: Dalia Halawani, Yiqun Wang. ✉e-mail: hongyan.zou@mssm.edu

and spinal cord injury (SCI) models. Mechanistically, AhR activation induced an injury regulon that reinforces protein homeostasis (proteostasis), whereas AhR loss shifted neurons towards elevated protein translation, metabolism and pro-growth signalling. We further identify cross-talk between AhR, HIF1α and ARNT in balancing neuronal stress adaptation with regenerative growth. Together, these findings establish AhR as a central regulator of the stress–growth switch after axotomy and suggest that targeting AhR may provide therapeutic opportunities for neural repair after SCI.

DRG neurons respond to AhR signalling

To examine transcriptional regulatory networks after axonal injury, we analysed early-response TFs identified in axotomized DRGs at 12 or 24 h after PL (regenerative) versus central lesion (non-regenerative)[15]. STRING analysis revealed extensive interconnections among established regeneration-associated TFs (ATF3[16], SOX11[17], JUN[18], SMAD1[15,19] and ATF4[20]) and TFs encoded by immediate early genes (EGR1 and CREM), but no functional links to AhR (Fig. 1a). A broader network of 39 TFs implicated in axon regeneration[21] likewise showed connectivity among SMAD, FOS, STAT and JUN, without association with AhR (Extended Data Fig. 1a).

As AhR is a ligand-activated bHLH-PAS TF, we examined DRG neuron responsiveness to AhR signalling using ITE (an endogenous indole-derived AhR agonist with broad disease-modulatory roles[22]) or CH-223191 (CH, a selective AhR antagonist[23]). Immunofluorescence (IF) staining of primary adult DRG neurons showed rapid nuclear translocation of AhR after 1.5 h ITE treatment, whereas CH promoted cytoplasmic retention (Fig. 1b). DRG neurons maintained in serum-free medium exhibited baseline nuclear AhR even after 4 days in culture, indicating endogenous ligand activity.

As a functional readout, we assessed expression of canonical AhR-target genes involved in detoxification (*Cyp1a1, Cyp1b1*) or negative feedback (*Ahrr*) (Fig. 1c). Reverse transcription–quantitative PCR (RT–qPCR) analysis confirmed induction of these genes by ITE and suppression by CH (Fig. 1d). In vivo intraperitoneal (i.p.) ITE injections for 3 days similarly upregulated *Cyp1a1* and *Cyp1b1* in DRGs, with a trend towards increased *Ahrr* (Extended Data Fig. 1b). Western blotting showed elevated CYP1B1 protein levels after in vivo ITE stimulation and an electrophoretic shift in AhR, consistent with post-translational modification (Fig. 1e). IF further confirmed AhR nuclear localization in DRG neurons after 2 days of ITE treatment, with minimal signal in glia (Fig. 1f).

Small interfering RNA (siRNA)-mediated knockdown of *Ahr* in adult DRG neurons, validated by RT–qPCR and IF (Fig. 1g), resulted in downregulation of AhR-target genes (Extended Data Fig. 1c). Analysis of mouse nervous system single-cell RNA-sequencing (scRNA-seq) data[24] confirmed expression of *Ahr*, *Hif1a* and *Arnt* across central nervous system (CNS) and peripheral nervous system (PNS) neuronal populations (Extended Data Fig. 1d). Together, these results establish that DRG neurons are responsive to ligand-mediated AhR signalling.

AhR inhibition enhances axon outgrowth

To investigate AhR function in adult DRG neurons, we performed neurite outgrowth assays. Neurons with *Ahr* knockdown extended significantly longer neurites than the controls (mean length of the longest neurite, 233 µm versus 193 µm, a 21% increase; Fig. 1h). Consistently, pharmacological modulation showed opposing effects, with AhR antagonists promoting and AhR agonists shortening neurite extension (Extended Data Fig. 1e).

Similar effects were observed in CNS neurons, including mouse neonatal cortical neurons and human induced neurons (iNs) derived from embryonic stem cells (Extended Data Fig. 1f–h). A broader pharmacological screen in human iNs confirmed dose-dependent effects of AhR antagonists and agonists (Extended Data Fig. 1i). Notably, StemRegenin1 (SR1), an AhR antagonist, was independently identified in an unbiased high-throughput screen for compounds enhancing neurite outgrowth in mouse adult cortical neurons[25], increasing neurite length by 28% and initiation by 58% (Extended Data Fig. 1j).

To further corroborate these findings, we generated tamoxifen-inducible neuronal *Ahr* conditional knockout (Ahr^{cKO}) mice by crossing $Ahr^{fl/fl}$ mice with $Thy1\text{-}cre^{ERT2/eYFP}$ (SLICK-H) mice (Fig. 1i). eYFP expression confirmed widespread neuronal targeting in DRG neurons and sciatic axons (Extended Data Fig. 2a), and efficient recombination was validated using the *Rosa26-LSL-Sun1-GFP* (INTACT) reporter line (Extended Data Fig. 2b). Genotyping and RNA-seq confirmed excision of *Ahr* exon 2 specifically in DRGs, with loss of exon 2 reads but preservation of distal exons, findings corroborated by RT–qPCR (Extended Data Fig. 2c–e). IF confirmed the loss of nuclear AhR in primary DRG neurons from Ahr^{cKO} mice (Fig. 1i). Of note, AhR protein levels appeared much higher in neurons than in glia (Extended Data Fig. 2f,g). Similarly, AhR protein was largely absent from DRG neurons of ITE-treated Ahr^{cKO} mice, while glial AhR expression was unchanged (Extended Data Fig. 2g).

Functionally, Ahr^{cKO} DRG neurons extended markedly longer neurites compared with the controls at 24 h after seeding (mean length of the longest neurite, 393 µm versus 232 µm, a 70% increase; Fig. 1j), consistent with the results from siRNA knockdown and pharmacological inhibition.

We next examined the in vivo efficacy of AhR antagonists SR1 and BAY-2416964 (BAY). Notably, 3 day i.p. injection of BAY but not SR1 resulted in longer neurites of seeded DRG neurons, reflective of specific in vivo pharmacokinetics or pharmacodynamics of different compounds (Fig. 1k,l). In vivo treatment with AhR agonist ITE did not cause shorter neurites (Fig. 1m), consistent with the self-limiting nature of AhR signalling by multiple negative-feedback loops. Together, both genetic and pharmacological approaches demonstrate that AhR inhibition can promote axon elongation across species and neuronal subtypes.

Early induction of AhR in DRGs after PL

To investigate AhR signalling in the conditioning lesion paradigm, we performed RNA-seq analysis of axotomized DRGs after PL, using contralateral DRGs to control for anaesthesia, pain or other systemic effects (Fig. 2a). Pathway analysis revealed enrichment of xenobiotic metabolism and hypoxia pathways after PL (Fig. 2b). Consistently, *Ahr*, *Hif1a*, *Arnt* and AhR targets (*Cyp1b1* and *Tiparp*), were upregulated after PL (Fig. 2c and Supplementary Table 1), whereas *Cyp1a1* and *Ahrr* showed low expression levels in sciatic DRGs.

Time-course RT–qPCR confirmed early induction of *Ahr* and *Arnt* at 12 h after PL, persisting to 48 h. *Hif1a* was induced slightly later, peaking at 24 h and returning to the baseline by 48 h (Fig. 2d). *Cyp1b1* and *Tiparp* followed a similar pattern to *Ahr* and *Arnt*, while *Ahrr* remained unchanged. scRNA-seq analysis[26] further verified induction of *Ahr*, *Hif1a* and *Arnt* across major DRG neuron subtypes from 12 to 72 h after PL (Extended Data Fig. 2h).

Western blot analysis confirmed AhR upregulation in sciatic DRGs as early as 6 h after PL, increasing by 12 h, peaking at 1–3 days post-injury (d.p.i.), and persisting at 14 d.p.i., paralleling ATF3, a marker of conditioning lesion[16] (Fig. 2e). AhR displayed an upward band shift at 12–24 h, similar to agonist-induced modification. In comparison, HIF1α protein was transiently induced, detectable at 12 h, peaking at 1 d.p.i. and declining by 3 d.p.i. Consistent with AhR activity, CYP1B1 protein showed transient induction from 6 hours post-injury (h.p.i.) to 3 d.p.i. These results indicate that PL triggers early but transient AhR activation, despite persistent AhR expression, consistent with rapid feedback attenuation of signalling[8].

AhR ablation enhances axon regeneration

We next examined the in vivo effects of neuronal *Ahr* deletion on axon regeneration using the sciatic nerve lesion (SNL) paradigm. IF staining

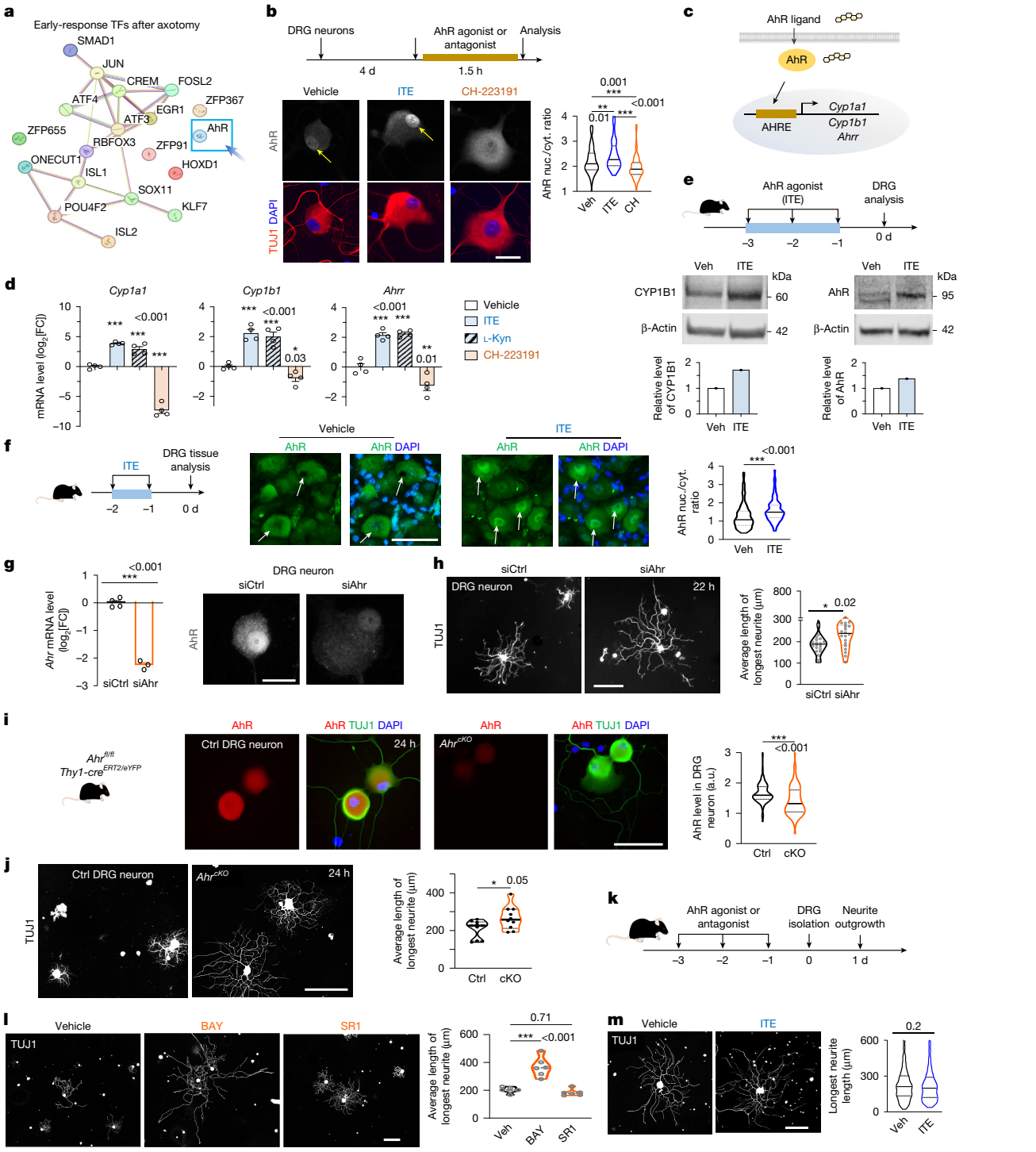

Fig. 1 | DRG neurons respond to AhR, which restricts axon outgrowth. **a**, STRING analysis shows no direct link between AhR and regeneration-associated TFs. **b**, Cytoplasm (cyt.) to nucleus (nuc.) AhR shuttling in cultured DRG neurons after 1.5 h exposure to ITE or CH (10 μM). $n = 100$ neurons per condition. d, days; Veh, vehicle. **c**, Ligand-mediated AhR activation induces target genes through the AHRE. **d**, RT–qPCR analysis of DRG neurons after 24 h agonist or antagonist treatment (25 μM). $n = 4$ cultures. FC, fold change. **e**, Immunoblot analysis of DRGs after in vivo ITE treatment (10 mg per kg, i.p.) showing CYP1B1 induction and AhR electrophoretic mobility shift. Quantification of the presented immunoblot is shown; the experiment was repeated three times with similar results. **f**, IF analysis showing increased nuclear AhR in DRG neurons from ITE-treated mice (arrows). $n = 10$ neurons per DRG from 9 sciatic DRGs, 3 mice per group. **g**, RT–qPCR and IF analysis confirm *Ahr* knockdown in primary DRG neurons 48 h after siRNA. $n = 4$ cultures. Ctrl, control. **h**, Neurite outgrowth in cultured adult DRG neurons. The mean longest neurite from $n = 20$ fields (>50 neurons each) is shown across 4 cultures. **i**, IF analysis showing reduced AhR in DRG neurons from Ahr^{cKO} mice 2 weeks after tamoxifen (100 mg per kg, 5 days, i.p.). $n = 15$ control and 16 Ahr^{cKO} neurons from random fields; 2 cultures. a.u., arbitrary units. **j**, Neurite outgrowth in DRG neurons from control and cKO mice. $n = 10$ fields across 2 cultures from 4 mice per genotype. **k**–**m**, Schematic (**k**) and quantification and imaging (**l**,**m**) of neurite outgrowth of DRG neurons from mice treated with AhR agonist (**m**) or antagonist (**l**). $n = 6$ random fields across independent cultures (**l**), and $n = 466$ (vehicle) and 533 (ITE) neurons from 3 mice per condition (**m**). Data are mean ± s.e.m. The violin plots show the median and quartiles. Statistical analysis was performed using one-way analysis of variance (ANOVA) with Dunnett's correction (**b**, **d** and **l**), unpaired two-tailed *t*-tests (**f**, **g** and **m**) and Mann–Whitney two-tailed *t*-tests (**h**–**j**). Scale bars, 20 μm (**g**), 25 μm (**b**), 50 μm (**f** and **i**), 100 μm (**m**) and 200 μm (**h**, **j** and **l**). $^*P \le 0.05$, $^{**}P \le 0.01$, $^{***}P \le 0.001$.

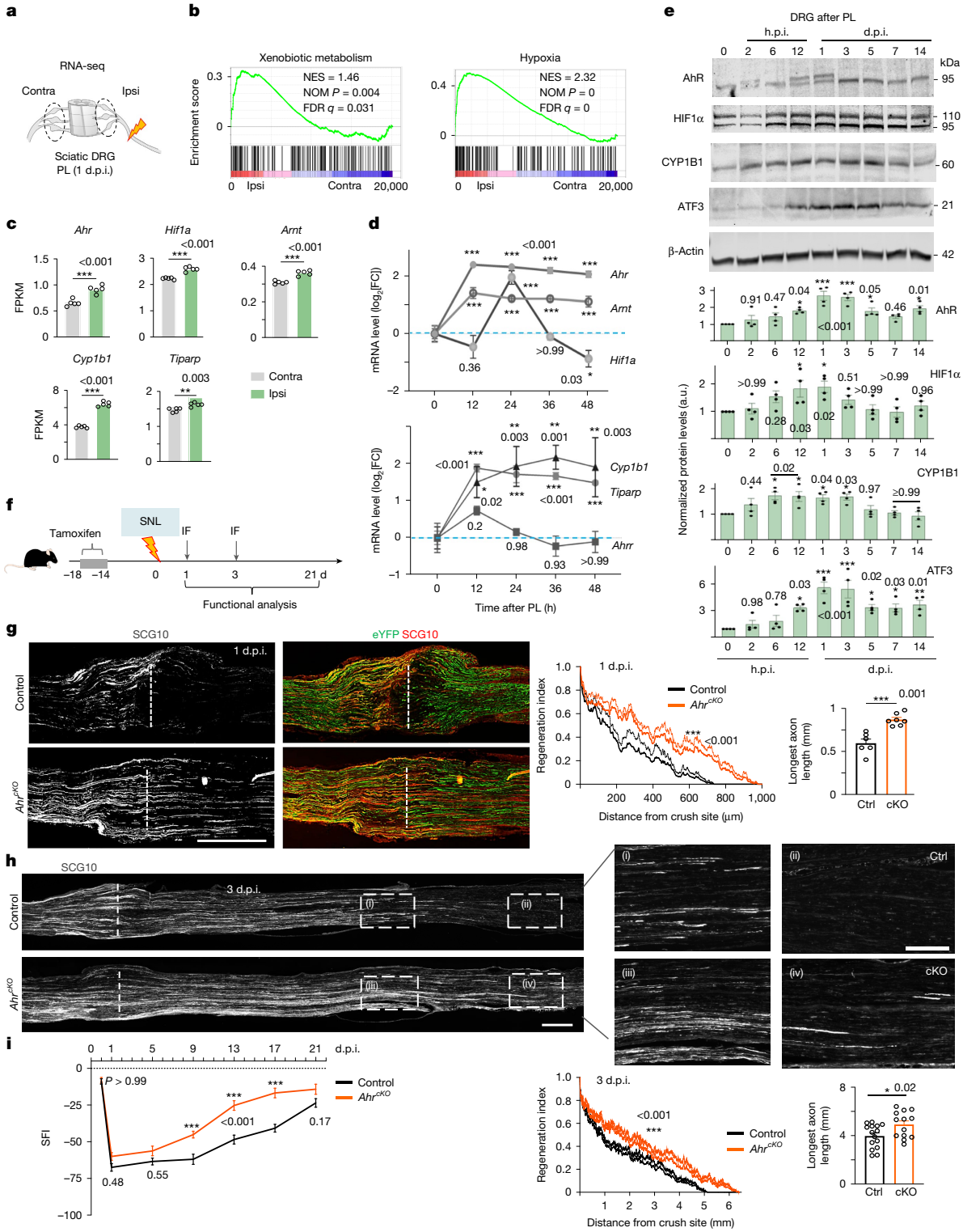

Fig. 2 | Neuronal *Ahr* deletion enhances axon regeneration after sciatic nerve injury. a, Design of RNA-seq experiment to compare ipsilateral (Ipsi) and contralateral (Contra) sciatic DRGs (L4–L6) of wild-type mice at 1 d.p.i. after PL. **b**, Gene set enrichment analysis (GSEA) showing enrichment of xenobiotic metabolism and hypoxia pathways in ipsilateral versus contralateral DRGs after PL. Statistical significance is reported as normalized enrichment scores (NES), nominal (NOM) *P* values and false-discovery rate (FDR)-adjusted *q* values derived from permutation testing; conventional parametric test statistics are not applicable. **c**, mRNA reads in ipsilateral and contralateral DRGs at 1 d.p.i. $n = 5$ DRG samples per condition. FPKM, fragments per kb transcript per million reads. **d**, Time-course RT–qPCR analysis of DRGs after PL. $n = 3$ mice, each with pooled L4–L6 DRGs per timepoint. **e**, Immunoblotting of DRG tissues at successive timepoints after PL. β-Actin was used as the loading control. $n = 4$ mice per timepoint. **f**, The SNL paradigm. **g**,**h**, IF analysis of regenerating axons (SCG10$^+$) traversing the SNL site (the dashed line indicates the centre) at 1 (**g**) and 3 (**h**) d.p.i. $n = 6$ (control) and 7 (cKO) mice at 1 d.p.i.; $n = 15$ (control) and 13 (cKO) mice at 3 d.p.i. For the regeneration index, statistical analysis was performed using two-way ANOVA with Bonferroni correction. The maximal axon length distal to the lesion centre was analysed using unpaired two-tailed Student's *t*-tests. **i**, SFI measurement shows enhanced recovery in *Ahr*^{cKO} mice at 9, 13 and 17 d.p.i. $n = 5$ mice per group. Data are mean ± s.e.m. Statistical analysis was performed using unpaired two-tailed *t*-tests (**c**), one-way ANOVA with Dunnett's correction (**d** and **e**) and two-way ANOVA with Bonferroni multiple-test correction (**i**). Scale bars, 200 μm (**h** (right)) and 500 μm (**g** and **h** (left)).

for SCG10, a marker of regenerating sensory axons[27], revealed more and longer axons extending beyond the crush site in Ahr^{cKO} compared with the controls at 1 d.p.i. (869 µm versus 594 µm, approximately a 50% increase) and 3 d.p.i. (5.8 mm versus 4.8 mm, around a 20% increase) (Fig. 2f–h), suggesting that *Ahr* deletion primes DRG neurons for rapid pro-repair activation.

After sciatic crush, both groups initially exhibited toe flexion deficits and weight-bearing failure but, from 9–17 d.p.i., Ahr^{cKO} mice showed a significantly improved sciatic functional index (SFI) (Fig. 2i). Neuronal *Ahr* deletion did not impair baseline motor–sensory performance in ladder walking or tactile sensitivity assays, either after short-term (2–5 weeks) or long-term (14 months) AhR ablation (Extended Data Fig. 2i).

The peripheral nerve regeneration phenotype was confirmed in $Ahr^{fl/fl}$ Nes^{cre} mice (*Nes* is a promoter element of *nestin*), with near-complete ablation of AhR proteins in DRG and brain by western blot analysis (Extended Data Fig. 3a). AhR proteins were robustly increased in axotomized DRGs at 3 d.p.i., which was blunted in Ahr^{cKO} mice although still mildly elevated compared with the naive state, suggesting immune AhR expression (Extended Data Fig. 3b). After sciatic crush, Ahr^{cKO} mice exhibited more and longer $SCG10^+$ axons beyond the lesion at 2 d.p.i., reflected in higher regeneration index and maximal axon length (1.44 mm versus 1.06 mm, a 36% increase) (Extended Data Fig. 3c). Functional recovery was accelerated, with earlier toe spreading, higher SFI from 9–21 d.p.i. and improved hindpaw reinnervation by $PGP9.5^+$ axons at 21 d.p.i. (Extended Data Fig. 3d,e). Ahr^{cKO} mice remained viable and fertile with no baseline deficits (Extended Data Fig. 3f), in contrast to constitutive *Ahr* knockouts, which develop demyelination and inflammation phenotypes[28].

The pro-regenerative effect was preserved in aged mice when *Ahr* cKO was induced at 14 months before SNL (Extended Data Fig. 4a,b). By contrast, *Ahr* deletion or pharmacological inhibition applied after SNL onset did not enhance axon regrowth (Extended Data Fig. 4c,d), indicating that early priming is required to gain over the robust intrinsic regenerative ability of DRG neurons after peripheral nerve injury.

We next examined whether neuronal AhR ablation could enhance CNS regeneration (Fig. 3a). Thoracic T8 contusion SCI produced comparable injury parameters in control and Ahr^{cKO} mice (Extended Data Fig. 5a). IF analysis at 35 d.p.i. revealed more neurofilament H-positive ($NF\text{-}H^+$) axon bundles traversing the dorsal spinal cord in Ahr^{cKO} mice (Fig. 3b,c), and ascending $CGRP^+$ sensory axons in the dorsal column showed greater abundance at and rostral to the lesion site in Ahr^{cKO} mice (Fig. 3d). Correspondingly, Ahr^{cKO} mice displayed superior motor–sensory recovery during 5 weeks of post-injury recovery, with higher Basso mouse scale (BMS) scores in open-field locomotion, fewer ladder-walking errors and improved tactile sensitivity (Fig. 3e and Supplementary Videos 1–6). Lesion size, demarcated by GFAP and CSPG, was unaffected (Extended Data Fig. 5b).

As a proof of principle, mice treated with the AhR inhibitor SR1 after SCI onset showed improved BMS scores from 14 d.p.i. onward, sustained through 35 d.p.i., accompanied by improved performance in ladder walking and von Frey filament assays (Extended Data Fig. 5c–e and Supplementary Videos 7–12). Collectively, neuronal AhR ablation enhances axonal regrowth and functional recovery after both peripheral and CNS injury.

Gut microbial depletion has no effect

AhR stability and cytoplasmic retention are regulated by HSP90, XAP2 (encoded by *Aip*) and p23 (encoded by *Ptges3*) (Extended Data Fig. 5f). RNA-seq analysis of DRGs revealed modest changes in these genes at 1 d.p.i. after PL, while RT–qPCR detected reduced *Aip* and *Ptges3* at 36 h, supporting early AhR activation after PL (Extended Data Fig. 5g,h).

We examined the L-kynurenine (L-Kyn) pathway as a potential AhR ligand source[29]. Transcriptome analysis of sciatic DRGs showed minimal changes in key enzymes converting tryptophan to L-Kyn or kynurenic acid at 1 d.p.i. after PL, with slight upregulation of *Kmo* and modest downregulation of *Kyat3*; *Ido1*, *Ido2* and *Tdo2* expression was low (Extended Data Fig. 5i,j). RT–qPCR analysis at 36 h revealed *Kyat1* downregulation and no change in *Kmo* (Extended Data Fig. 5k), indicating no major transcriptional regulation of this pathway in axotomized DRGs.

To test microbial contributions to AhR activation[30], the gut microbiome was depleted with antibiotics for 18 days before SNL, but neurite outgrowth in cultured DRG neurons and axon regeneration in vivo were unaffected (Extended Data Fig. 6a–c). Indole-3-propionate (IPA) is a gut microbiota-derived metabolite linked to axon regeneration through neutrophil chemotaxis[31]. IPA can also act as an AhR ligand to modulate sepsis and neuroinflammation[32,33], although the serum concentration of IPA is far below the levels needed to produce an AhR-dependent physiological effect[34]. In primary DRG neurons, IPA treatment did not enhance neurite outgrowth and even reduced outgrowth at higher concentrations (Extended Data Fig. 6d).

As *Thy1-creERT2/eYFP* is also expressed in enteric neurons, the gut immune composition was assessed, and no significant changes were detected (Extended Data Fig. 6e–g). Neuronal AhR ablation also did not alter immune responses after peripheral nerve injury: IF of sciatic DRGs showed no differences in $CD45^+$ leukocytes, $CD206^+$ myeloid cells, $CD68^+$ phagocytes, $IBA1^+$ macrophages or $PU.1^+$ myeloid lineage cells under naive or axotomized conditions (Extended Data Fig. 7a,b). Other immune subsets ($NK1.1^+$ natural killer cells, $Ly6G^+$ neutrophils, and $CD4^+$ and $CD8^+$ T cells) were rare and unaffected. At the nerve crush site, $F4/80^+$ macrophages and $SOX10^+$ Schwann cells showed comparable density and distribution in Ahr^{cKO} and control mice (Extended Data Fig. 7c). These results suggest that enhanced axonal regrowth in Ahr^{cKO} mice arises from neuron-intrinsic mechanisms rather than altered immune or Schwann cell responses.

AhR regulon enforces proteostasis

To assess pathways impacted by neuronal *Ahr* deletion after axonal injury, we profiled DRG transcriptomes from Ahr^{cKO} and control mice at 1 d.p.i. after PL ($n = 5$ per group), using contralateral DRGs to control for systemic effects (Fig. 3f and Supplementary Tables 1 and 2). Principal component analysis (PCA) revealed that injury status, rather than genotype, accounted for the largest variance (PC1, 43%), with ipsilateral and contralateral DRGs forming distinct clusters, whereas genotype did not segregate samples either before or after injury (Extended Data Fig. 8a). Thus, *Ahr* cKO induced pathway-specific, rather than global, transcriptomic shifts.

In control mice, *Ahr* was robustly upregulated in ipsilateral DRGs at 1 d.p.i.; in Ahr^{cKO} mice, *Ahr* was reduced, more prominently in contralateral DRGs ($\log_2[FC] = -0.24$, $P = 0.01$) than ipsilateral ($\log_2[FC] = -0.10$, $P = 0.27$), reflecting glial induction after PL (Extended Data Fig. 8b). Comparison of ipsilateral versus contralateral DRGs identified 2,658 peripheral lesion-induced differentially expressed genes (PL-DEGs) in Ahr^{cKO} mice and 2,501 in control mice, with 1,802 overlapping genes showing largely concordant directionality, although some displayed amplitude shifts or divergent responses (Extended Data Fig. 8c and Supplementary Table 3). Canonical xenobiotic pathways (AhR, PXR, CAR) were suppressed in Ahr^{cKO} DRGs, with widespread transcriptional remodelling of 134 curated xenobiotic metabolism genes after PL (Fig. 3g and Supplementary Table 4).

To capture broader AhR-dependent effects, we calculated response-shift scores (RSSs; $\log_2[FC\ (cKO)] - \log_2[FC\ (control)]$) across PL-DEGs. Applying a threshold of $|RSS| \geq 0.3$, we identified 1,431 AhR-responsive genes (898 negative, 533 positive RSSs; Fig. 3h and Supplementary Table 5). Enrichment analysis highlighted translational control, including tRNA processing, mitochondrial tRNA and rRNA maturation, and extracellular matrix interactions, with most genes showing negative RSS, consistent with AhR as a transcriptional activator (Fig. 3i,j).

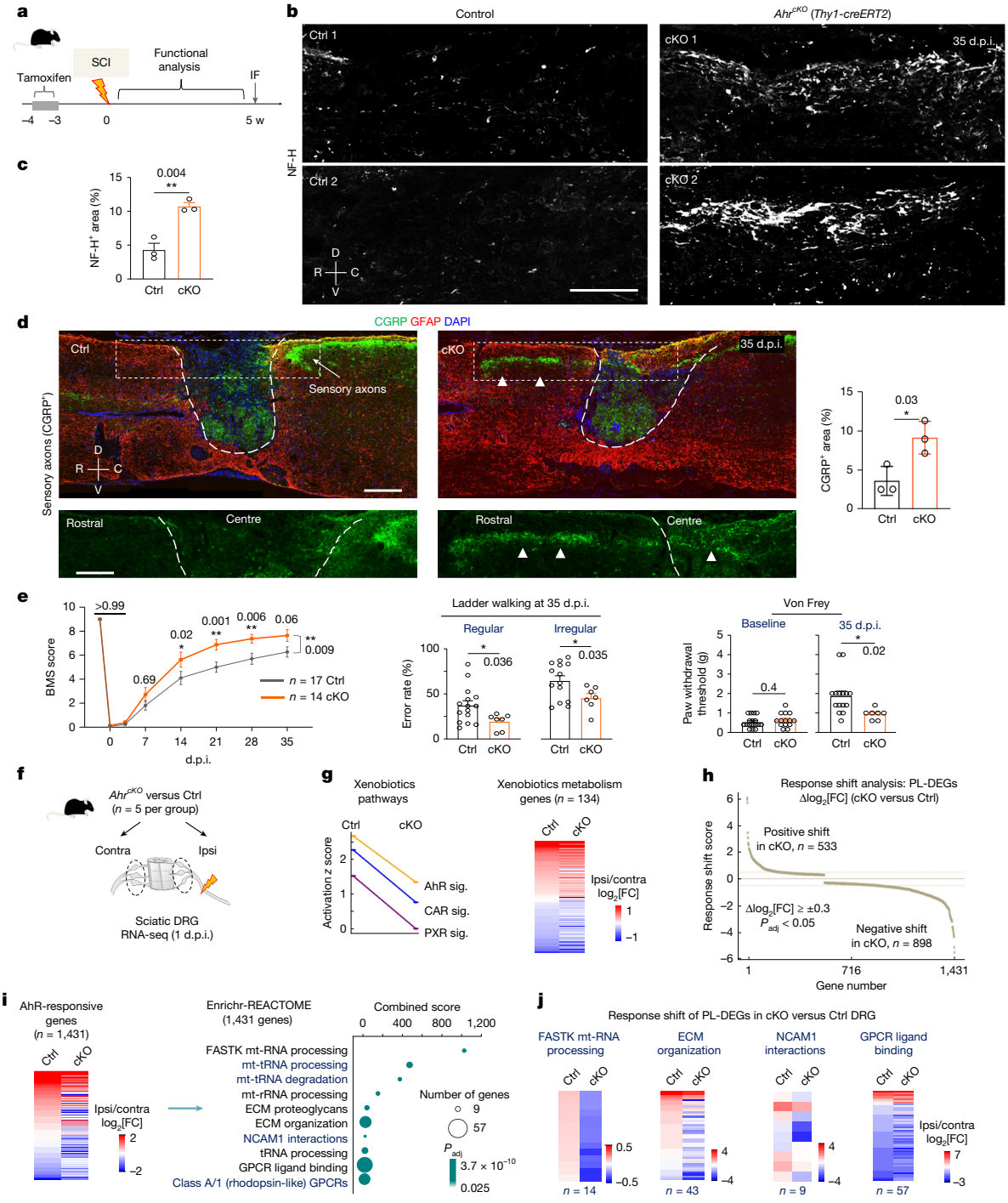

Fig. 3 | Neuronal *Ahr* deletion enhances axon regrowth and functional recovery after SCI. a, The experimental timeline of the T8 contusion injury study. w, weeks. **b**,**c**, IF analysis of NF-H (**b**) and quantification (**c**) shows an increase in axons traversing the lesion site in Ahr^{cKO} mice at 35 d.p.i. $n = 3$ mice per group. Data are mean ± s.e.m. C, caudal; D, dorsal; R, rostral; V, ventral. **d**, IF analysis of CGRP revealing more sensory axons in the dorsal column of the injury site in Ahr^{cKO} mice, with multiple fibres detected in regions rostral to lesion centre (arrowheads). $n = 3$ mice per group. Data are mean ± s.e.m. **e**, Locomotor function scored based on BMS, the ladder walking assay and the von Frey filament assay demonstrates improved motor and sensory performance in Ahr^{cKO} mice. For BMS, $n = 17$ control and 14 cKO mice per datapoint. For regular ladder walking and von Frey assays, $n = 15$ for control and 7 for Ahr^{cKO} mice; for irregular rung ladder assay, $n = 14$ for control and 7 for Ahr^{cKO} mice. *P* values are shown for difference in BMS score between control and cKO mice at each timepoint (numbers above datapoints) and across all timepoints (number next to bracket). Data are mean ± s.e.m. **f**, RNA-seq analysis of ipsilateral and contralateral sciatic DRGs (L4–L6) from Ahr^{cKO} mice and littermate controls at 1 d.p.i. $n = 5$ per group. **g**, Xenobiotic metabolism pathways were suppressed in Ahr^{cKO} mice. The heat map shows AhR-dependent response shifts of 134 xenobiotic metabolism genes after PL. sig., signalling. **h**, The response shift score ($\log_2$[FC (cKO)]) − $\log_2$[FC (control)]) across PL-DEGs. Adjusted *P* (P_{adj}) values (Benjamini–Hochberg FDR correction; $|\Delta\log_2[FC]| \geq 0.3$, adjusted $P < 0.05$) were derived from the original differential expression analyses before calculating RSSs. **i**, The heat maps show changes for 1,431 AhR-responsive genes at 1 d.p.i. after PL (left). Enrichr pathway analysis of AhR-responsive genes after PL (right). Pathways with adjusted $P < 0.1$ (Fisher's exact test, Benjamini–Hochberg correction) were retained and ranked by combined score. ECM, extracellular matrix; mt, mitochondrial. **j**, Gene expression changes in the enriched pathways between control and cKO after PL. Statistical analysis was performed using unpaired two-tailed *t*-tests (**c**, **d** and **e** (ladder walking and von Frey)) and two-way ANOVA with Tukey's correction (**e** (BMS)). Scale bars, 100 µm (**b** and **d** (bottom)) and 200 µm (**d** (top)).

G-protein-coupled receptor (GPCR) signalling was also enrfiched, which can rapidly modulate protein synthesis[35]. For validation, we performed RT–qPCR analysis of ipsilateral versus contralateral DRGs from control and Ahr^{cKO} mice. This confirmed AhR-dependent transcriptional shifts in genes linked to protein homeostasis and metabolic adaptation (Extended Data Fig. 8d,e).

We next analysed the AhR-responsive genes by applying ChEA3 analysis, an integrative TF enrichment analysis tool that combines chromatin immunoprecipitation–sequencing (ChIP–seq) datasets, gene co-expression and TF–gene co-occurrence. This revealed 132 putative AhR direct targets, 87% of which showed negative RSS in Ahr^{cKO} mice (Extended Data Fig. 8f and Supplementary Table 6). These genes were strongly enriched in translational pathways, anchoring the broader AhR-dependent signatures. Additional pathways included BDNF, HIF1α, senescence, autophagy and metabolism of vitamin B12, selenium, folate and low-density lipoprotein (Extended Data Fig. 8g).

Comparative IPA of PL-associated transcriptomes (ipsilateral versus contralateral) between genotypes showed that control DRGs preferentially engaged proteostasis pathways, including rRNA processing, ribosome assembly and clearance of metabolites, proteins and organelles (leucine degradation, pexophagy, mitochondrial proteolysis, glutaryl-CoA degradation and mRNA decay; Extended Data Fig. 8h,j). By contrast, Ahr^{cKO} DRGs activated growth-promoting signalling (neurexin, NGF, insulin, PDGF and L1CAM), protein sorting, histone modification and lipid biosynthesis (Extended Data Fig. 8i,j).

Elevated protein synthesis by *Ahr* cKO

Transcriptomic analyses suggested that AhR upregulation after axotomy reinforces protein quality control and proteostasis, whereas its loss reprograms the injury response towards biosynthesis and pro-growth signalling (Fig. 4a). Pathway analysis implicated mitochondrial–cytosolic cross-talk, with cytosolic tRNA charging and ubiquitination upregulated and mitochondrial pathways suppressed in cKO (Fig. 4b). Protein trafficking pathways, including autophagy and endocytosis, were also activated (Fig. 4b).

To directly assess the impact of AhR ablation on neuronal protein synthesis, we performed a puromycin (a tyrosyl-tRNA analogue) incorporation assay to label elongating peptides (Fig. 4c). The assay showed robust, dose-dependent puromycin signals in cultured DRG neurons (Fig. 4d). Puromycin incorporation was markedly higher in neurons than in glia, indicating greater neuronal translational activity (Fig. 4d).

At 24 h after seeding of primary DRG cultures (axotomy occurs during dissociation), Ahr^{cKO} neurons exhibited around 25% higher puromycin incorporation compared with the controls (Fig. 4e). Consistently, in vivo puromycin injection at 1 d.p.i. after PL revealed significantly greater labelling (24% increase) in Ahr^{cKO} DRG neurons, indicating enhanced de novo protein synthesis after axotomy (Fig. 4f).

To further investigate the underlying mechanisms, analysis of DRG transcriptomes for translational regulators showed reduced expression of *Eif4ebp1* (an inhibitor of 5′-cap-dependent translation), *Sesn2* and *Castor1* (amino acid sensors and inhibitors of mTOR activity), along with decreased *Rps14* (encoding a 40S ribosomal subunit protein) (Fig. 4g,h). Concordantly, phosphorylated ribosomal protein S6 ($p\text{-}RPS6^{Ser235/236}$), a marker of mTOR activity, was elevated in Ahr^{cKO} DRG neurons at 1 d.p.i. after PL (Fig. 4i). Together, AhR constrains neuronal translation by limiting mTOR signalling and ribosome processing, whereas AhR loss unleashes neuron-intrinsic protein synthesis to support regenerative growth.

AhR–HIF1α cross-talk in axon regeneration

As AhR and HIF1α share ARNT as a dimerization partner, we tested whether HIF1α activity is required for the regenerative phenotype of Ahr^{cKO} neurons (Fig. 5a). Pharmacological inhibition of HIF1α translation with KC7F2 reduced HIF1α abundance and abolished the growth advantage of Ahr^{cKO} neurons (Fig. 5b and Extended Data Fig. 9a). Similarly, siRNA-mediated *Arnt* knockdown eliminated the axon-promoting effect of *Ahr* deletion, reducing neurite length to control levels (Fig. 5c), indicating engagement of the HIF1α–ARNT pathway during axon regrowth in Ahr^{cKO} DRG neurons.

By contrast, conditional deletion of *Arnt* ($Arnt^{fl/fl}Thy1\text{-}creERT2/eYFP$) did not impair baseline or PL-induced axon outgrowth in primary DRG neurons, nor in vivo regeneration at 3 d.p.i. after SNL (Extended Data Fig. 9b–e). Thus, although ARNT is required for enhanced outgrowth in Ahr^{cKO} neurons, ARNT-deficient neurons can compensate through alternative pathways.

To further examine AhR–HIF1α interplay, ChEA3 analysis of AhR-responsive PL-DEGs identified 121 candidate HIF1α targets, nearly half overlapping with putative AhR targets (Fig. 5d). The 58 overlapping genes were enriched for RNA and protein metabolism, cellular stress responses, senescence and axon growth-promoting pathways including HIF1α, p53, MAPK and PI3K–AKT signalling (Fig. 5d and Supplementary Table 6). These results support transcriptional cross-talk between AhR and HIF1α after axotomy, with AhR loss shifting the balance from stress responses and proteostasis towards HIF1α-mediated metabolic adaptation and pro-growth signalling.

Integration with epigenomic data implicated 5hmC-mediated regulation in this cross-talk. Our previous genome-wide profiling of PL-induced differentially hydroxymethylated regions (DhMRs) identified 1,036 sites (predominantly within gene bodies[5,36]), enriched for bHLH-PAS TF motifs including HIF1α, ARNT and BMAL1, but not AhR (Extended Data Fig. 9f,g). Notably, 40% of DhMRs contained HIF1α-response elements (HREs), corresponding to 766 genes, with 27 overlapping AhR-responsive PL-DEGs that are enriched in amino sugar metabolism, ubiquitination, neuronal migration and WNT signalling (Extended Data Fig. 9h and Supplementary Table 7). Thus, a subset of AhR-responsive PL-DEGs may operate through DhMRs or HREs in Ahr^{cKO} DRGs after axotomy.

Further linking AhR and 5hmC, Ahr^{cKO} DRGs showed elevated 5hmC levels after axotomy (Extended Data Fig. 9i). Given that BMAL1 gates regenerative responses through 5hmC and that xenobiotic metabolism and AhR signalling were among the top pathways in the *Bmal1* cKO regulon (Extended Data Fig. 9j), BMAL1 may act upstream of AhR signalling. Together, these data position AhR, HIF1α and BMAL1 as interconnected bHLH-PAS TFs coordinating transcriptional and epigenomic responses to axonal injury (Extended Data Fig. 9k).

Stress–growth balance by AhR inhibition

To define the putative neuronal AhR regulon, we leveraged published scRNA-seq data from DRG neurons collected between 6 h and 14 days after PL[37], and identified 98 AhR-associated genes (Extended Data Fig. 10a,b and Supplementary Table 8). In contrast to regeneration-associated TFs (ATF3, SOX11, SMAD1, CREB1, MYC and JUN) or TFs encoded by early response genes (EGR1 and FOS), AhR was predicted to be inactivated during axon regeneration, consistent with its inhibitory role. Pathway analysis of the AhR regulon ($n = 98$) highlighted translational control, including RNA polymerase III (RNA Pol III) transcriptional termination (Extended Data Fig. 10c). Notably, the regulon included *Nfia* and *Nfib*, nuclear factors that are involved in RNA Pol III transcriptional termination that have AHREs in their promoters (Extended Data Fig. 10d).

The PL-associated TFs also included stress-response TFs ATF4 and ATF6 (Extended Data Fig. 10b). ATF4 is a regulator of the integrated stress response (ISR) activated by chronic endoplasmic reticulum (ER) stress or amino acid deprivation[38], or elevated levels of uncharged tRNA[39] (Fig. 5e). scRNA-seq showed that *Atf4*, *Atf6* and *Xbp1*, the latter encoding another regulator of acute ER stress, were broadly induced in DRG neurons and contained AHREs in their promoters (Fig. 5e and

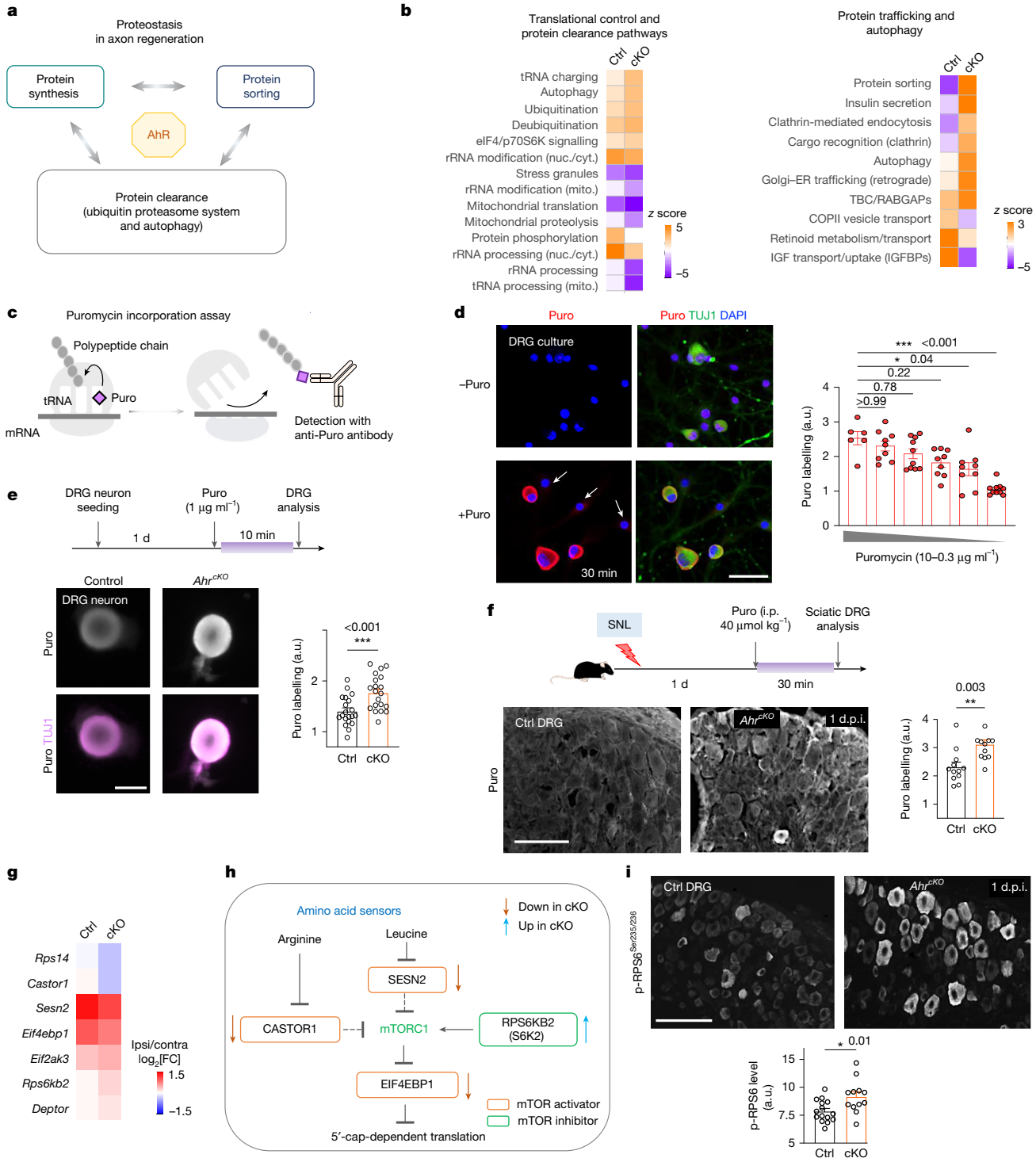

Fig. 4 | AhR controls proteostasis and global protein synthesis after axotomy. a, Model of AhR-dependent control of proteostasis in axon regeneration. **b**, Comparative IPA of PL-DEGs (ipsilateral versus contralateral DRGs) reveals enrichment of pathways related to translational regulation and proteostasis. IGFBPs, IGF binding proteins; mito., mitochondrial. **c**, Schematic of the puromycin (Puro) incorporation assay to assess de novo protein synthesis. **d**, Assay validation. IF analysis of DRG cultures shows specific puromycin labelling in TUJ1$^+$ neurons after 30 min exposure, with minimal labelling in TUJ1$^-$ glial cells (arrows). Quantification shows dose-dependent incorporation. The mean puromycin fluorescence intensity is shown from $n = 10$ random fields across three independent cultures. **e**, IF images show significantly higher puromycin labelling in *Ahr*^{cKO} neurons compared with in the controls. The average intensity of $n = 20$ random fields of independent DRG neuron cultures is shown from 2 mice per group. **f**, IF images show increased puromycin incorporation in *Ahr*^{cKO} neurons compared with the controls. Data are the mean fluorescence intensity from $n = 3$ sciatic DRGs (L5); 3 mice per genotype. **g**, Key translational regulators identified as AhR-responsive by RNA-seq analysis of ipsilateral and contralateral DRGs at 1 d.p.i. after PL ($n = 5$ per condition; $P_{adj} < 0.05$). **h**, Diagram of translational regulators affected by *Ahr* cKO after PL. **i**, IF analysis showing elevated p-RPS6 (Ser235/236) in *Ahr*^{cKO} DRG neurons at 1 d.p.i., with minimal signal in glia. The mean p-RPS6 fluorescence intensity is shown from random fields of sciatic DRGs. $n = 5$ (control) and $n = 4$ (cKO) mice. Data are mean ± s.e.m. Statistical analysis was performed using one-way ANOVA with Dunnett's multiple-comparisons correction (**d**) and unpaired two-tailed *t*-tests (**e**, **f** and **i**). Scale bars, 25 µm (**e**), 50 µm (**d**) and 100 µm (**f** and **i**).

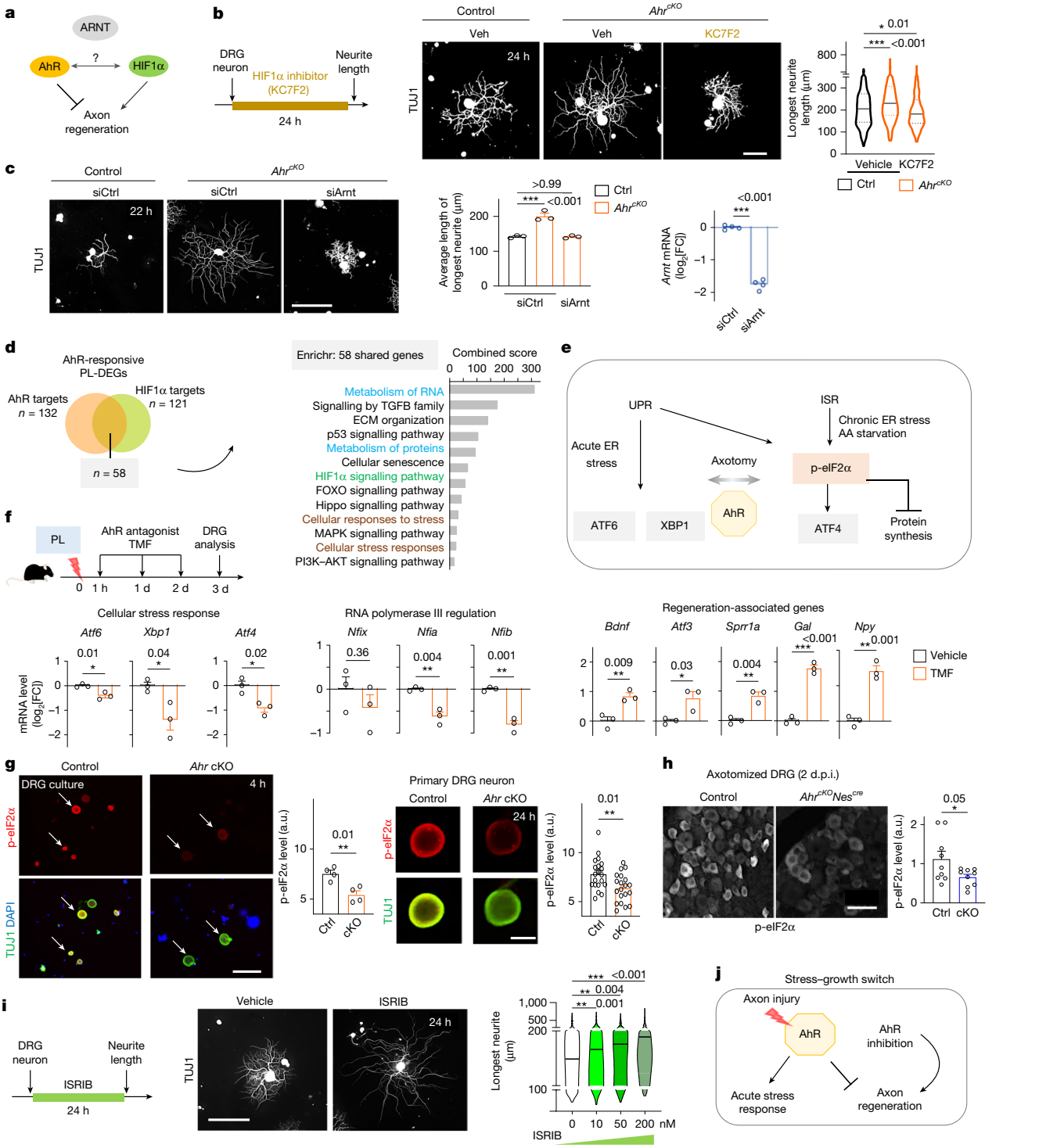

Fig. 5 | The growth-promoting effect of *Ahr* deletion requires cross-talk with HIF1α. a, Schematic of AhR–HIF1α interactions in regulating axon regeneration. **b**, IF images show that HIF1α inhibitor KC7F2 (10 μM) abolished neurite outgrowth advantage of Ahr^{cKO} DRG neurons. The violin plots show the median and quartiles. $n = 250–408$ neurons per condition from independent cultures of 2 mice per genotype. **c**, IF analysis showing that siRNA knockdown of *Arnt* reverted enhanced neurite growth of Ahr^{cKO} neurons. Data are the mean longest neurite from $n = 10$ fields across 3 cultures per genotype. Right, RT–qPCR analysis confirmed reduced *Arnt* mRNA 48 h after siRNA. $n = 4$ per group. **d**, Venn diagram showing 58 genes overlapping between putative AhR and HIF1α targets, which were analysed for pathway enrichment. Blue, metabolism; brown, stress response; green, hypoxia. **e**, Diagram of stress sensors linked to protein synthesis. AA, amino acid. **f**, DRG RT–qPCR analysis after post-injury injection of AhR antagonist TMF (10 mg per kg, i.p., 3 days) shows that TMF suppressed stress-associated genes and Pol III regulators while inducing regeneration-associated genes. $n = 3$ samples from 3 mice, each pooled from L4–L6 DRGs. **g**, IF analysis of p-eIF2α (Ser51) in primary DRG neurons. $n = 4$ (4 h) and $n = 20$ (24 h) fields. **h**, Reduced p-eIF2α levels in DRG neurons in Ahr^{cKO} mice at 2 days after PL. $n = 3$ mice per genotype. **i**, The dose-dependent effect of ISR inhibitor (ISRIB) on neurite outgrowth. $n = 625$ (0 nM), 462 (10 nM), 474 (50 nM) and 427 (200 nM) neurons from 4 cultures. **j**, Working model: AhR restricts axonal regrowth while promoting acute stress responses. Data are mean ± s.e.m. Statistical analysis was performed using one-way ANOVA with Dunnett's correction (**b**, **c** (left) and **i**) and unpaired two-tailed *t*-tests (**c** (right), **f**, **g** and **h**). Scale bars, 25 μm (**g** (right)), 50 μm (**h**), 100 μm (**b** and **g** (left)) and 200 μm (**c** and **i**).

Extended Data Fig. 10e,f). Validation studies showed that post-injury administration of the AhR inhibitor TMF in vivo suppressed expression of the genes encoding these stress-responsive TFs and RNA Pol III regulators (*Nfia, Nfib*), while upregulating regeneration-associated genes (*Bdnf*, *Atf3*, *Sprr1a*, *Gal*, *Npy*), as well as *Stmn1* (encoding SCG10), *Tead1* (Hippo signalling) and other AHRE- and HRE-bearing genes including *Sox9, Rest* and *Cdk6* (Fig. 5f and Extended Data Fig. 10g,h).

Phosphorylation of eIF2α at Ser51 (p-eIF2α) is a central integration hub of the unfolded protein response (UPR) and ISR that suppresses protein synthesis[38] (Fig. 5e). *Ahr*^{cKO} neurons exhibited reduced p-eIF2α levels (indicative of reduced translational stress), both in vitro (4 h and 24 h after seeding) and in vivo after PL (Fig. 5g,h). Functionally, pharmacological blockade of the ISR with ISRIB significantly enhanced neurite outgrowth of DRG neurons in a dose-dependent manner (Fig. 5i).

Discussion

Neurons must balance environmental stressors with regenerative demands after axonal injury. Here we identify AhR as a central regulator of this stress–growth switch. AhR induction after axotomy engages proteostasis and the ISR to suppress translation and preserve tissue integrity but constrains regeneration; conversely, AhR inhibition relieves this brake and redirects neuronal responses towards metabolic adaptation and pro-regrowth signalling, promoting axon regeneration in both PNS and CNS injury models (Fig. 5j).

AhR is best known as a xenobiotic sensor regulating detoxification enzymes and transporters, although evolutionary evidence suggests this function emerged later from an ancestral neuronal role[40]. AhR is broadly expressed in the nervous system[40,41], where it regulates axon and dendrite branching in invertebrates[41,42] and, in mammals, restrains dendritic complexity and neuronal differentiation[43,44]. Our findings extend this framework, establishing AhR as a neuronal brake on axon regeneration, consistent with computational predictions from unbiased high-throughput screens[45].

Mechanistically, AhR induction after axotomy rewires gene programs that reinforce protein quality control and proteostasis. After PL, AhR activation is transient and dampened by feedback loops, enabling an acute stress response while timely freeing ARNT for HIF1α signalling. This transition is required for enhanced regeneration of *Ahr*^{cKO} DRG neurons by shifting transcriptional programs towards metabolic and regenerative pathways.

AhR activation engages broad proteostasis and UPR and ISR programs, spanning RNA Pol III activity, ribosome biogenesis, autophagy, ubiquitination, protein trafficking and mitochondrial–cytosolic cross-talk, whereas AhR loss activates growth-promoting pathways (HIF1α, BDNF and PI3K–AKT) and micronutrient metabolism. The AhR injury regulon includes genes encoding stress-associated TFs (ATF4, ATF6 and XBP1), and AhR-deficient neurons display increased protein synthesis, elevated p-RPS6 and reduced p-eIF2α, consistent with relief from translational suppression. We further identify cross-talk among bHLH-PAS TFs in coordinating stress adaptation and regeneration. Circadian factor BMAL1 appears upstream of xenobiotic pathways, while HIF1α also regulates circadian programs[46]. Integration with epigenomic datasets revealed overlap between AhR-responsive PL-DEGs and PL-induced DhMRs enriched for HIF1α motifs. *Ahr* cKO increased 5hmC in DRG neurons after axotomy, suggesting transcriptome rewiring through epigenetic remodelling. AhR may also control transcription through non-AHRE interactions[47].

Functionally, *Ahr* cKO enhanced axon regrowth and motor–sensory recovery after both PNS and CNS lesions. Post-injury treatment with the AhR antagonist SR1 phenocopied genetic deletion, although effects were limited in the CNS paradigm. Given the reported effects of SR1 on haematopoietic stem cells[48], further studies are needed to define drug specificity, target engagement, pharmacokinetics and potential side effects. Future axonal tracing studies will also help to determine whether distinct neuronal subtypes respond similarly to AhR inhibition.

The identity of endogenous AhR ligands may arise from local metabolites, systemic inflammation or oxidative stress. Although antibiotic-mediated microbiome depletion did not overtly affect nerve regeneration, additional gut-related influences on AhR activity cannot be excluded. Natural AhR polymorphisms also shape ligand sensitivity across species[8], raising the possibility that regenerative capacity varies with diet, pathogens or genetic background. More broadly, our findings align with protective effects of AhR inhibition reported in stroke[49], Huntington's disease[50], gut–lung[51] and endothelial responses[52,53].

In summary, our work establishes AhR as a brake on axon regeneration that integrates transcriptional, metabolic and epigenetic programs to enforce proteostasis at the expense of regenerative growth. By positioning AhR within a regulatory network alongside HIF1α and BMAL1, these findings open avenues to target stress–growth plasticity to improve nervous system repair.

Online content

Any methods, additional references, Nature Portfolio reporting summaries, source data, extended data, supplementary information, acknowledgements, peer review information; details of author contributions and competing interests; and statements of data and code availability are available at https://doi.org/10.1038/s41586-026-10295-z.

1. Zheng, B. & Tuszynski, M. H. Regulation of axonal regeneration after mammalian spinal cord injury. *Nat. Rev. Mol. Cell Biol.* **24**, 396–413 (2023).
2. Song, Y. et al. A glycolytic shunt via the pentose phosphate pathway is a metabolic checkpoint for nervous system sensory homeostasis and axonal regeneration. *Cell* **189**, 1211–1227 (2026).
3. Coumoul, X. et al. The aryl hydrocarbon receptor: structure, signaling, physiology and pathology. *Signal Transduct. Target. Ther.* **11**, 20 (2026).
4. Bersten, D. C., Sullivan, A. E., Peet, D. J. & Whitelaw, M. L. bHLH-PAS proteins in cancer. *Nat. Rev. Cancer* **13**, 827–841 (2013).
5. Halawani, D. et al. Circadian clock regulator Bmal1 gates axon regeneration via Tet3 epigenetics in mouse sensory neurons. *Nat. Commun.* **14**, 5165 (2023).
6. Cho, Y. et al. Activating injury-responsive genes with hypoxia enhances axon regeneration through neuronal HIF-1α. *Neuron* **88**, 720–734 (2015).
7. Rothhammer, V. & Quintana, F. J. The aryl hydrocarbon receptor: an environmental sensor integrating immune responses in health and disease. *Nat. Rev. Immunol.* **19**, 184–197 (2019).
8. Avilla, M. N., Malecki, K. M. C., Hahn, M. E., Wilson, R. H. & Bradfield, C. A. The Ah receptor: adaptive metabolism, ligand diversity, and the xenokine model. *Chem. Res. Toxicol.* **33**, 860–879 (2020).
9. Schiering, C. et al. Feedback control of AHR signalling regulates intestinal immunity. *Nature* **542**, 242–245 (2017).
10. Semenza, G. L. Hypoxia-inducible factors in physiology and medicine. *Cell* **148**, 399–408 (2012).
11. Gradin, K. et al. Functional interference between hypoxia and dioxin signal transduction pathways: competition for recruitment of the Arnt transcription factor. *Mol. Cell. Biol.* **16**, 5221–5231 (1996).
12. Mascanfroni, I. D. et al. Metabolic control of type 1 regulatory T cell differentiation by AHR and HIF1-α. *Nat. Med.* **21**, 638–646 (2015).
13. Richardson, P. M. & Issa, V. M. Peripheral injury enhances central regeneration of primary sensory neurones. *Nature* **309**, 791–793 (1984).
14. Neumann, S. & Woolf, C. J. Regeneration of dorsal column fibers into and beyond the lesion site following adult spinal cord injury. *Neuron* **23**, 83–91 (1999).
15. Zou, H., Ho, C., Wong, K. & Tessier-Lavigne, M. Axotomy-induced Smad1 activation promotes axonal growth in adult sensory neurons. *J. Neurosci.* **29**, 7116–7123 (2009).
16. Seijffers, R., Mills, C. D. & Woolf, C. J. ATF3 increases the intrinsic growth state of DRG neurons to enhance peripheral nerve regeneration. *J. Neurosci.* **27**, 7911–7920 (2007).
17. Norsworthy, M. W. et al. Sox11 expression promotes regeneration of some retinal ganglion cell types but kills others. *Neuron* **94**, 1112–1120 (2017).
18. Ruff, C. A. et al. Neuronal c-Jun is required for successful axonal regeneration, but the effects of phosphorylation of its N-terminus are moderate. *J. Neurochem.* **121**, 607–618 (2012).
19. Parikh, P. et al. Regeneration of axons in injured spinal cord by activation of bone morphogenetic protein/Smad1 signaling pathway in adult neurons. *Proc. Natl Acad. Sci. USA* **108**, E99–E107 (2011).
20. Oñate, M. et al. Activation of the unfolded protein response promotes axonal regeneration after peripheral nerve injury. *Sci. Rep.* **6**, 21709 (2016).
21. Michaelevski, I. et al. Signaling to transcription networks in the neuronal retrograde injury response. *Sci. Signal.* **3**, ra53 (2010).
22. Song, J. et al. A ligand for the aryl hydrocarbon receptor isolated from lung. *Proc. Natl Acad. Sci. USA* **99**, 14694–14699 (2002).

23. Zhao, B., Degroot, D. E., Hayashi, A., He, G. & Denison, M. S. CH223191 is a ligand-selective antagonist of the Ah (Dioxin) receptor. *Toxicol. Sci.* **117**, 393–403 (2010).
24. Zeisel, A. et al. Molecular architecture of the mouse nervous system. *Cell* **174**, 999–1014 (2018).
25. Sefiani, A., Rusyn, I. & Geoffroy, C. G. Novel adult cortical neuron processing and screening method illustrates sex- and age-dependent effects of pharmaceutical compounds. *Sci. Rep.* **12**, 13125 (2022).
26. Renthal, W. et al. Transcriptional reprogramming of distinct peripheral sensory neuron subtypes after axonal injury. *Neuron* **108**, 128–144 (2020).
27. Shin, J. E., Geisler, S. & DiAntonio, A. Dynamic regulation of SCG10 in regenerating axons after injury. *Exp. Neurol.* **252**, 1–11 (2014).
28. Juricek, L. et al. AhR-deficiency as a cause of demyelinating disease and inflammation. *Sci. Rep.* **7**, 9794 (2017).
29. Cuartero, M. I. et al. L-kynurenine/aryl hydrocarbon receptor pathway mediates brain damage after experimental stroke. *Circulation* **130**, 2040–2051 (2014).
30. Hubbard, T. D., Murray, I. A. & Perdew, G. H. Indole and tryptophan metabolism: endogenous and dietary routes to ah receptor activation. *Drug Metab. Dispos.* **43**, 1522–1535 (2015).
31. Serger, E. et al. The gut metabolite indole-3 propionate promotes nerve regeneration and repair. *Nature* **607**, 585–592 (2022).
32. Huang, Z. B. et al. Gut microbiota-derived indole 3-propionic acid partially activates aryl hydrocarbon receptor to promote macrophage phagocytosis and attenuate septic injury. *Front. Cell. Infect. Microbiol.* **12**, 1015386 (2022).
33. Sun, J. et al. Microbiota-derived metabolite Indoles induced aryl hydrocarbon receptor activation and inhibited neuroinflammation in APP/PS1 mice. *Brain Behav. Immun.* **106**, 76–88 (2022).
34. Morgan, E. W. et al. Contribution of circulating host and microbial tryptophan metabolites toward Ah receptor activation. *Int. J. Tryptophan Res.* **16**, 11786469231182510 (2023).
35. Tréfier, A. et al. G protein-coupled receptors as regulators of localized translation: the forgotten pathway? *Front. Endocrinol.* **9**, 17 (2018).
36. Loh, Y. E. et al. Comprehensive mapping of 5-hydroxymethylcytosine epigenetic dynamics in axon regeneration. *Epigenetics* **12**, 77–92 (2017).
37. Wang, K. et al. Single-cell transcriptomic analysis of somatosensory neurons uncovers temporal development of neuropathic pain. *Cell Res.* **31**, 904–918 (2021).
38. Costa-Mattioli, M. & Walter, P. The integrated stress response: from mechanism to disease. *Science* **368**, eaat5314 (2020).
39. Harding, H. P. et al. Regulated translation initiation controls stress-induced gene expression in mammalian cells. *Mol. Cell* **6**, 1099–1108 (2000).
40. Huang, X., Powell-Coffman, J. A. & Jin, Y. The AHR-1 aryl hydrocarbon receptor and its co-factor the AHA-1 aryl hydrocarbon receptor nuclear translocator specify GABAergic neuron cell fate in *C. elegans*. *Development* **131**, 819–828 (2004).
41. Qin, H. & Powell-Coffman, J. A. The *Caenorhabditis elegans* aryl hydrocarbon receptor, AHR-1, regulates neuronal development. *Dev. Biol.* **270**, 64–75 (2004).
42. Crews, S. T. & Brenman, J. E. Spineless provides a little backbone for dendritic morphogenesis. *Genes Dev.* **20**, 2773–2778 (2006).
43. de la Parra, J. et al. AhR deletion promotes aberrant morphogenesis and synaptic activity of adult-generated granule neurons and impairs hippocampus-dependent memory. *eNeuro* https://doi.org/10.1523/ENEURO.0370-17.2018 (2018).
44. Dever, D. P. et al. Aryl hydrocarbon receptor deletion in cerebellar granule neuron precursors impairs neurogenesis. *Dev. Neurobiol.* **76**, 533–550 (2016).
45. Geeven, G. et al. LLM3D: a log-linear modeling-based method to predict functional gene regulatory interactions from genome-wide expression data. *Nucleic Acids Res.* **39**, 5313–5327 (2011).
46. O'Connell, E. J., Martinez, C. A., Liang, Y. G., Cistulli, P. A. & Cook, K. M. Out of breath, out of time: interactions between HIF and circadian rhythms. *Am. J. Physiol. Cell Physiol.* **319**, C533–C540 (2020).
47. Ohtake, F. et al. Modulation of oestrogen receptor signalling by association with the activated dioxin receptor. *Nature* **423**, 545–550 (2003).
48. Boitano, A. E. et al. Aryl hydrocarbon receptor antagonists promote the expansion of human hematopoietic stem cells. *Science* **329**, 1345–1348 (2010).
49. Chen, W. C. et al. Aryl hydrocarbon receptor modulates stroke-induced astrogliosis and neurogenesis in the adult mouse brain. *J. Neuroinflamm.* **16**, 187 (2019).
50. García-Lara, L., Pérez-Severiano, F., González-Esquivel, D., Elizondo, G. & Segovia, J. Absence of aryl hydrocarbon receptors increases endogenous kynurenic acid levels and protects mouse brain against excitotoxic insult and oxidative stress. *J. Neurosci. Res.* **93**, 1423–1433 (2015).
51. Major, J. et al. Endothelial AHR activity prevents lung barrier disruption in viral infection. *Nature* **621**, 813–820 (2023).
52. Wiggins, B. G. et al. Endothelial sensing of AHR ligands regulates intestinal homeostasis. *Nature* **621**, 821–829 (2023).
53. Shah, K. et al. Cell-intrinsic aryl hydrocarbon receptor signalling is required for the resolution of injury-induced colonic stem cells. *Nat. Commun.* **13**, 1827 (2022).

Methods

Animals

Animal procedures were conducted under a protocol approved by the Institutional Animal Care and Use Committee of Icahn School of Medicine at Mount Sinai (IPROTO202200000184). All of the mice were maintained on the C57BL/6J genetic background for at least three generations. Animals were housed in a specific-pathogen-free barrier facility under a 12 h–12 h light–dark cycle with ad libitum access to food and water. Ambient temperature was maintained at approximately 18–23 °C with relative humidity of 40–60%. Mice were group-housed (up to five per cage) in corn bedding-lined cages with standard pellet chow and water bottles and were acclimatized to the facility for at least 2 weeks before experimentation. All of the mice used in the study were young adults (aged <30 weeks), unless otherwise indicated.

Mouse strains were obtained from The Jackson Laboratory: C57BL/6J (JAX, 000664); *Tg(Thy1-cre/ERT2-eYFP)HGfng* (JAX, 012708, known as SLICK-H)[54,55]; *B6.Cg-Tg(Nes-cre)1Kln/J* (JAX, 003771, known as Nes^{cre})[56]; $Ahr^{tm3.1Bra}$*/J* (JAX, 006203, known as Ahr^{fl})[57]; and *B6;129-Gt(ROSA)26Sor*$^{tm5(CAG-Sun1/sfGFP)Nat}$*/J* (JAX, 021039, known as INTACT)[58]; and $Arnt^{fl/fl}$ mice[59] were provided by F. Gonzalez.

The following primers were used for genotyping by PCR using mouse tail DNA: $Ahr^{fl/fl}$ mice: F1: GTCACTCAGCATTACACTTTCTA, F2: CAGTG GGAATAAGGCAAGAGTGA, R1: GGTACAAGTGCACATGCCTGC. Expected band sizes: 106 bp for wild-type allele, 140 bp for the floxed allele and 180 bp for the excised floxed allele. $Arnt^{fl/fl}$ mice: F1: TGCCAACAT GTGCCACCATGT, R1: GTGAGGCAGATTTCTTCCATGCTC. 290 bp for the wild-type allele, 340 bp for the *Arnt* floxed allele. Nes^{cre} mice: F1: CCGCTTCCGCTGGGTCACTGT, R1: TGAGCAGCTGGTTCTGCTCCT, R2: ACCGGCAAACGGACAGAAGCA. 379 bp for the wild-type allele, 229 bp for the transgenic *cre* allele. $Rosa26^{INTACT}$ mice: F1: GCACTTGCTCTCCC AAAGTC, R1: CATAGTCTAACTCGCGACACTG, R2: GTTATGTAACGCGG AACTCC. 557 bp for wild-type allele, 300 bp for the knock-in allele. $Thy1\text{-}creER^{T2}$ mice: F1: TCTGAGTGGCAAAGGACCTTAGG, R1: CGCTG AACTTGTGGCCGTTTACG, Int-F2: CAAATGTTGCTTGTCTGGTG, Int-R2: GTCAGTCGAGTGCACAGTTT. 200 bp for the wild-type allele, 300 bp for the transgenic *cre* allele.

Pharmacological treatments

To induce CreER-mediated cKOs, tamoxifen (Sigma-Aldrich, T5648) in corn oil (Sigma-Aldrich, C8267) was injected into adult mice i.p. (100 mg per kg) once daily for 5 days.

AhR agonists. 2-(1′H-indole-3′-carbonyl)-thiazole-4-carboxylic acid methyl ester (ITE; Tocris 1803), L-Kyn (Tocris 4393), 6-formylindolo [3,2-b]carbazole (FICZ; Tocris 5304) and norisoboldine (NOR; Selleckchem S9092) were reconstituted in DMSO. For in vitro studies, the applied concentrations are indicated in the main text. For in vivo experiments, ITE was diluted in 12.5% kolliphor/PBS (Sigma-Aldrich, C5135) to a final volume of 600 µl and injected i.p. at 10 mg per kg.

AhR antagonists. CH (Tocris, 3858), 6,2′,4′-trimethoxyflavone (TMF; Tocris, 3859), StemRegenin-1 (SR1; Selleckchem, S2858) and BAY (Selleckchem, S8995) were reconstituted in DMSO. For in vivo studies, TMF was further diluted in 12.5% kolliphor/PBS, and injected i.p. at 10 mg per kg (or, for SR1 and BAY[60], 25 mg per kg) using a Hamilton fine syringe (Hamilton, 80920).

HIF1α translational inhibition. KC7F2 (Cayman, 14123), a small-molecule inhibitor targeting HIF1α through translational control was used previously[61].

ISR inhibition. ISRIB (Sigma-Aldrich, 5.09584)[62] was reconstituted in DMSO.

Antibiotics treatment. Broad-spectrum depletion of gut microorganisms was performed according to a published protocol with minor modifications[63]. In brief, wild-type C57BL/6J mice received drinking water containing ampicillin sodium (1 g l^{-1}; Sigma-Aldrich, A9518), vancomycin hydrochloride (0.5 g l^{-1}; Sigma-Aldrich, V2002), neomycin sulfate (1 g l^{-1}; Sigma-Aldrich, N1876), metronidazole (1 g l^{-1}; Sigma-Aldrich, M1547), sucrose (50 g l^{-1}; Sigma-Aldrich, S0389) and acetic acid (4 mM) for 18 days before sciatic nerve crush. Solutions were provided ad libitum in light-protected bottles and replaced every third day.

Indole metabolite. 3-Indolepropionic acid (IPA; Selleckchem S4809) was dissolved in DMSO. As vehicle controls for drug treatments, either DMSO or DMSO dissolved in 12.5% kolliphor/PBS were used as appropriate.

SNL

Male and female mice, aged 8–18 weeks unless otherwise specified, were anaesthetized by isoflurane inhalation (5% for induction, 2% for maintenance). A small skin incision was made at mid-thigh using a scalpel blade after skin preparation and disinfection. To clearly expose the sciatic nerve, the fascial space between biceps femoris and gluteus superficialis muscles was opened gently without causing haemorrhage. The nerve was then freed from surrounding connective tissue under microscope, avoiding shearing or traction forces. For sciatic nerve crush model, the nerve was crushed with an Ultra-fine Hemostat (Fine Science Tools, 13020-12) for 15 s at the third click. For the sciatic nerve transection model, the nerve was cut with a 3 mm Vannas Spring Scissor (Fine Science Tools, 15000-00). For sham surgery, the sciatic nerve was exposed as described but left intact. Mouse skin was closed using the Reflex 7 mm Wound Closure System (Braintree Scientific, RF7 CS) after surgery. Mice were left to recover in a warm cage. All of the surgical instruments were autoclaved before surgery and aseptic techniques were maintained throughout.

SCI model

T7–T9 laminectomy was performed on 8-week-old mice (wild-type C57BL/6 female). The mice were then clamped using two pairs of Adson forceps before using the Infinite Horizon Impactor at 60 kdyn of force with a 2 s dwell time to induce a moderate T8 contusion and compression as described previously[64–66]. The muscles and skin were closed with 5.0 sutures, and the skin was sealed with Dermabond. After surgery, mice recovered in a warmed cage and were then moved to a normally temperate cage and provided with food and water ad libitum. All of the animals received subcutaneous injections of 1 ml saline, 10 mg per kg Baytril, and 0.05 mg per kg buprenorphine daily for the first week after surgery. All surgeries were performed in the morning (08:00–12:00) to limit potential circadian influence. Bladders were expressed manually twice daily. All drug administrations were performed by individuals blinded to the experimental groups.

DRG isolation

DRG dissections were conducted under a Nikon SMZ645 stereomicroscope. Euthanized mice were positioned supine and secured to a dissection pad. The ventral thoracic and abdominal skin and viscera were removed to expose the ventral spinal column using surgical scissors (Fine Science Tools, 14054-13) with tissue forceps (Fine Science Tools, 11021-12) for support. Ventral paraspinal muscles were cleared using spring scissors (Fine Science Tools, 15751-11) to visualize the lumbosacral nerve plexus. To expose the lumbosacral DRGs, ventral vertebral elements were removed using the same spring scissors, aided by octagon forceps (Fine Science Tools, 11042-08), while avoiding nerve transection. L4–L6 DRGs were then isolated by gently elevating the ganglion with Dumont #3 forceps (World Precision Instruments,

50037) and severing connecting nerves with Vannas spring scissors (Fine Science Tools, 15000-00).

Primary DRG neuron culture

Adult DRGs from adult C57BL/6J mice were dissected and placed into ice-cold DMEM/F12 (Gibco, 11330057). DRGs were washed three times with ice-cold calcium-free and magnesium-free HBSS (Gibco, 14175095) including 10 mM HEPES (Gibco, 15630106) before incubating in 0.3% collagenase I (Worthington, LS004196) for 90 min at 37 °C. DRGs were then washed three times with HBSS buffer with HEPES at room temperature, followed by additional digestion in 0.25% trypsin-EDTA (Gibco, 25200072) containing 50 μg ml^{-1} DNase I (Worthington, LK003172) for 30 min at 37 °C. Trypsinization was stopped with warm DMEM medium (Gibco, 10569044) containing 10% FBS (Gibco, 26140079) and DNase I. DRGs were dissociated by trituration with fire-polished Pasteur glass pipets (Fisherbrand, 13-678-20D). To remove myelin debris and cell clumps, a partial-purification step was performed by centrifugation through a BSA (Thermo Fisher Scientific, BP9700100) cushion. Specifically, the DRG suspension was mixed with 8 ml NS-A basal medium (NeuroCult 05750) and then 2 ml of 15% BSA in HBSS was added at the bottom of the 15 ml centrifuge tube followed by centrifugation at 1,000 rpm for 6 min. The supernatant was carefully removed and DRGs were resuspended in NS-A basal medium containing 2% B27 (Gibco, A3582801), 0.725% glucose, 0.5 mM L-glutamine and 0.4% antibiotic–antimycotic (Gibco, 15240062). DRG neurons were plated onto poly-L-ornithine-coated (Sigma-Aldrich, P4957) and laminin-coated (Gibco, 23017015) chamber slides or 6-well plates for subsequent experiments. siRNA-mediated knockdown studies were conducted as previously described with modifications[67]. Around 4,000 DRG neurons were resuspended in 1.5 ml of titration medium (without DNase I) and gently mixed with 0.5 ml of transfection complex containing 2 μl of DharmaFECT 2.0 (Dharmacon, T-2002-02) and 2 μl of siRNA at 20 μM stock concentration in Neurocult NB-A medium and seeded on PLO-/laminin-coated plates/coverslips. ON-TARGETplus SMART pool siRNA oligos were obtained from Dharmacon (*Ahr*, siRNA-L-044066-00; *Arnt*, siRNA-L-040639-01-0005; and non-targeting pool, D-001810-10-05).

Generation of induced human neurons

The studies using human embryonic stem cells were approved by the Embryonic Stem Cell Research Oversight Committee (ESCRO) at Icahn School of Medicine at Mount Sinai. The H9 human embryonic stem cell line (WA09) was acquired from WiCell through the Mount Sinai Stem Cell Core. Induced neurons were generated as described previously[5]. In brief, H9 embryonic stem cells were induced to neuroprogenitor cells (NPCs) using STEMDiff SMADi neural induction kit (Stem Cell Technologies, 08581). NPCs were passaged at a density of 1.2×10^6 in 2 ml of STEMdiff neural progenitor medium (Stem Cell Technologies, 05833). Mixed cortical neuron culture was induced from NPCs as described previously[68]. Differentiation medium contained BrainPhys medium (Stem Cell Technologies, 05790) with 1× N2 (Gibco, 17502048), 1× B27 (Invitrogen, 12587-010), 20 ng ml^{-1} brain-derived neurotrophic factor (BDNF, Peprotech 450-02), 20 ng ml^{-1} glial-derived neurotrophic factor (GDNF, Peprotech 450-10), 200 μM L-ascorbic acid (Stem Cell Technologies, 72132) and 250 μg ml^{-1} dibutyryl cyclic AMP sodium salt (db-cAMP, Stem Cell Technologies, 73884). Half of the medium volume was changed with fresh differentiation medium every other day for 10 to 13 days before analysis.

Mouse cortical neuron culture

The cortical adult neuron assay was conducted as described previously[25]. In brief, wild-type 6-week-old C57BL/6 male mice were euthanized using CO_2 and the cortex was isolated and transferred to a MACS C-tube, then dissociated using the Miltenyi gentleMACS octo-dissociator on a preset protocol. This was followed by the removal of debris and endothelial blood cells using the Mitlenyi MACS Adult Brain Dissociation Kit (Miltenyi Biotec, 130-107-677). Next, using the Adult Neuron Isolation Kit (Miltenyi Biotec, 130-126-603), according to the manufacturer's instructions, the negative fraction (fraction enriched with neurons) was collected and used for the cortical neurite outgrowth assay. High-content confocal imaging was carried out using the ImageXpress Micro Confocal (IXM) High-Content Imaging System (Molecular Devices).

For cultures of early postnatal cortical neurons, cortices from postnatal day 0–2 wild-type mouse pups were isolated after careful removal of meninges. Tissue was minced, washed in cold HBSS and dissociated using the Neural Tissue Dissociation Kit-T (Miltenyi, 130-094-802). After cell counting, 1×10^5 cells were seeded per well onto 24-well plates containing glass coverslips coated with poly-L-ornithine (Sigma-Aldrich, P4957) and laminin (Gibco, 23017015).

Neurite outgrowth assays

L4–L6 DRG neurons were seeded onto PLO-/laminin-precoated four-well chamber slides (Falcon, 10384501) at around 1,000–2,000 neurons per well. Neurons were fixed with ice-cold 4% PFA and stained with anti-tubulin β3 (TUJ1) to visualize outgrowing neurites.

For pharmacological experiments, DRG neurons from wild-type C57BL/6J mice were plated onto a PLO-/laminin-precoated six-well plate, using neurons from 8–10 DRGs per well. Neurons were cultured for 24 h with pharmacological AhR modulators. Cells were either fixed for IF staining or used directly for RNA lysis and RT–qPCR analysis.

A replating assay was performed on induced neurons between differentiation day 10 to 13 as described previously[5,69]. In brief, cells were washed twice with PBS and incubated in 0.025% trypsin for 5 min at 37 °C. Trypsin was gentle removed while keeping neurons attached and replaced with differentiation medium. Gentle pipetting was then carried out to dissociate the neurons followed by counting and seeding in 4-well chamber slides at a density of 55,000 cells per well in differentiation medium containing AhR agonists or antagonists for 1 day before analysis.

The adult mouse cortical neurite outgrowth assay was performed as described previously[25]. In brief, primary adult cortical neurons were seeded onto PDL-coated plastic-bottom plates (Greiner-Bio, 781091) at 10,000 cells per well for 2 days. SR1 (TargetMol T1831) and vehicle were added at the time of plating and left in the medium for 2 days without medium change. Neuronal medium consisted of MACS neuro media (Miltenyi Biotec, 130-093-570), 2 mM L-alanine-L-glutamine dipeptide (Sigma-Aldrich, G8541) and 1× B27 Plus supplement (Thermo Fisher Scientific, A3582801).

For postnatal mouse cortical neurite outgrowth assays, at seeding, cultures were treated with AhR modulators or vehicle control in Neurobasal-A medium (Gibco, 10888022) supplemented with 2% B27 Plus (Gibco, A3582801), 2 mM GlutaMAX-I (Gibco, 35050061), 5% FBS and 1% penicillin–streptomycin (Gibco, 15140122) and maintained at 37 °C with 5% CO_2. Neurons were fixed after 24 h for immunostaining, imaging and quantification of neurite length.

Puromycylation (SUnSET) assay for nascent protein synthesis

Puromycin dihydrochloride (MP Biomedicals, 210055280; Sigma-Aldrich, P8833) was dissolved in water to generate a 10 mg ml^{-1} stock solution. During optimization for neuronal cultures, puromycin was applied at 0.3–10 μg ml^{-1} for up to 30 min at 37 °C, followed by three washes with ice-cold PBS and IF analysis using an anti-puromycin antibodies. Vehicle-treated cultures served as negative controls and were processed in parallel. For experimental studies, DRG cultures from control or cKO mice were pulsed with 1 μg ml^{-1} puromycin in fresh medium for 10 min at 37 °C, washed twice with ice-cold PBS and analysed as described above.

In vivo puromycylation assay was performed as previously described[70,71]. Puromycin was prepared as a 4.8 mg ml^{-1} stock in PBS and administered i.p. at 21.8 mg per kg (0.040 μmol g^{-1}). Mice were

euthanized 30 min after injection; DRGs were dissected, fixed in 4% PFA for 1.5 h at 4 °C, and processed for IF analysis using anti-puromycin antibodies.

RNA isolation and RT–qPCR

Total RNA of cells or tissues was extracted using the RNeasy Plus Mini kit (Qiagen, 74134). For RNA collection from tissue, dissected DRGs were initially stored in RNAlater stabilization solution (Invitrogen, AM7024) and then homogenized in RLT Plus buffer including 1% β-mercaptoethanol using RNase-free disposable pellet pestles (Fisherbrand, 12-141-364). For RNA collection from cells, cell cultures were washed once with PBS and then lysed by vigorous pipetting. Genomic DNA was eliminated through a gDNA eliminator column according to the manufacturer's instructions. RNA was eluted in RNase-free water and stored at −80 °C. cDNA was prepared with the SuperScript III First-Strand Synthesis System (Invitrogen, 18080051) from equal amounts of RNA (approximately 200 ng from DRG tissues and 500 ng from cell culture for each reaction). RT–qPCR was performed with PerfeCTa SYBR Green FastMix Rox (Quanta Bioscience, 95073-012) with an ABI 7900HT quantitative PCR system (Applied Biosystems) at the Mount Sinai qPCR CoRE. *Hprt1* was used as the house-keeping gene to normalize RT–qPCR results. Data were analysed using SDS software v.2.4. A list of the primers for RT–qPCR analysis is provided in Supplementary Table 9.

Western blot

Sciatic (L4–L6) DRGs were collected and immediately frozen in liquid nitrogen and stored at −80 °C for later analysis. Tissues were homogenized and lysed with RIPA buffer (Sigma-Aldrich, R0278) containing EDTA-free protease inhibitor cocktail (Roche, 04693159001) and phosSTOP (Roche, 4906845001). The frozen DRGs in a 1.5 ml tube were disrupted with RNase-free disposable pellet pestles (Fisherbrand, 12-141-364) on ice. Then, 1 U μl^{-1} benzonase nuclease (Millipore, E1014) was added to lysis buffer. The samples were mixed on a rotator at 4 °C for 30 min and then spun on a tabletop centrifuge at 13,000 rpm for 10 min to remove undissolved pellet. An equal volume of 4× LDS sample buffer (Invitrogen, NP0008) was added to the lysates, which were then boiled at 95 °C for 5 min. The lysates from an equal number of DRGs were loaded and separated by electrophoresis on 4–12% ExpressPlus gels (Genscript, M41210), followed by transfer to a PVDF membrane. Membranes were blocked in Intercept blocking buffer (LI-COR Biosciences, 927-70001) at room temperature for 1 h and subsequently incubated with primary antibodies diluted with Intercept antibody diluent (LI-COR Biosciences, 927-75001) at 4 °C overnight. The blots were washed with PBST (five times for 5 min) and incubated with secondary antibodies at room temperature for 1 h. Bands were detected using the Odyssey Infrared Imaging System (LI-COR Biosciences) and the band intensity was quantified using Image Studio software (v.5.2.5; LI-COR Biosciences).

Primary antibodies for western blots were as follows: anti-AHR (rabbit, 1:1,000, Enzo, BML-SA210, AB_10540536), anti-CYP1B1 (rabbit, 1:1,000, Invitrogen, PA5-95277, AB_2807081), anti-HIF1α (rabbit, 1:500, Novus, NB100-479, AB_10000633), anti-ATF3 (rabbit, 1:1,000, Santa Cruz, sc-188, AB_2258513) and anti-β-actin (mouse, 1:10,000, Sigma-Aldrich, A1978, AB_476692). Secondary antibodies for western blots were as follows: 800CW donkey anti-rabbit IgG (1:10,000, LI-COR Biosciences, 926-32213) and 680RD donkey anti-mouse IgG (1:10,000, LI-COR Biosciences, 926-68072).

IF analysis

For IF analysis of cultured cells, cultures were washed once with PBS and then fixed in 4% ice-cold PFA for 15 min. For IF of cryosections of DRG tissues, sciatic nerves and spinal cords, tissues were fixed in 4% ice-cold PFA/PBS for 12 h, washed in PBS, soaked in 30% sucrose overnight and then embedded in OCT compound (Thermo Fisher Scientific, 23-730-571). Cryosections were cut at a thickness of 12 µm and placed onto SuperFrost Plus slides (VWR, 48311-703) and stored at −20 °C before analysis. The sections were washed with PBS and incubated in blocking buffer containing 5% normal donkey serum (Jackson Immunoresearch, 017-000-121) and 0.3% Triton X-100 (Acros Organics, 9002-93-1) in PBS for 1 h at room temperature. Primary antibodies were diluted in antibody dilution buffer containing 1% BSA (Fisher BioReagents, BP9700100) and 0.3% Triton X-100 in PBS and incubated at 4 °C overnight. Alexa-coupled secondary antibodies were diluted in antibody dilution buffer and added on sections after three washes with PBS and incubated for 1 h at room temperature. DAPI (Invitrogen, D1306) was used for nuclear counterstaining (1:1,000). Slides were washed three times with PBS and mounted with Fluromount G (Southern Biotech, 0100-01). Whole-mount staining of footpad was performed as previously described[5]. In brief, the footpad skin of the injured hind paw was dissected, cleaned from connective tissue, washed with PBS and fixed in 4% PFA overnight at 4 °C. Tissue was rinsed ten times for 30 min with PBS containing 0.3% Triton-X (0.3% PBST) followed by incubation with primary antibody in blocking buffer (0.3% PBST containing 5% goat serum and 20% DMSO) for 5 days at room temperature with gentle shaking. Tissue was washed ten times for 30 min with 0.3% PBST and incubated with secondary antibody in blocking buffer for 3 days at room temperature with gentle shaking. Subsequently, tissue was washed ten times for 30 min with 0.3% PBST, dehydrated in 50% methanol for 5 min, 100% methanol for 20 min, and cleared in a 1:2 benzyl alcohol: benzyl benzoate mix overnight at room temperature.

Primary antibodies for IF were as follows: anti-AHR (rabbit, 1:300, Enzo, BML-SA210, AB_10540536), anti-ATF3 (rabbit, 1:300, Santa Cruz, sc-188, AB_2258513), anti-tubulin β3 (TUJ1, mouse, 1:1,000, BioLegend, 801201, AB_2313773), anti-tubulin β3 (D71G9, rabbit, 1:300, Cell Signaling, 5568S, AB_10694505), anti-SCG10/STMN2 (rabbit, 1:1,000, Novus, NBP1-49461, AB_10011569), anti-GFP (chicken, 1:1,000, Aves Lab, GFP-1020, AB_10000240), anti-IBA1 (rabbit, 1:1,000, Wako, 019-19741, AB_839504), anti-pS6 ribosomal protein-S235/236 (rabbit, 1:300, Cell Signaling, 2211, AB_331679), anti-5hmC (rabbit, 1:500, Active Motif, 39769, AB_10013602), anti-CD8a (rat, 1:100, Invitrogen, 14-0081-82, AB_467087), anti-CD4 (rat, 1:100, Invitrogen, 14-0041-82, AB_467063), anti-CD68 (rat, 1:100, BioLegend, 137002, AB_2044004), anti-CD45 (rat, 1:100, BD Pharmingen, 550539, AB_2174426), anti-PU1 (E.388.3) (rabbit, 1:300, Thermo Fisher Scientific, MA5-15064, AB_10986949), anti-F4/80 (rat, 1:300, Thermo Fisher Scientific, 14-4801-81, AB_467557), anti-CD206 (goat, 1:200, R&D systems, AF2535, AB_2063012), anti-SOX10 (goat, 1:50, R&D systems, AF2864, AB_442208), anti-PGP9.5 (rabbit, 1:800, Neuromics, RA12103, AB_2315126), anti-NF-H (chicken, EMD Millipore, AB5539, 1:1,000, AB_11212161), anti-CSPG (CS-56) (mouse, Sigma-Aldrich, C8035, 1:100, AB_476879), anti-GFAP (chicken, Aves Labs, GFAP, 1:500, AB_2858088), anti-puromycin (mouse, DSHB, PMY-2A4, 1:100, AB_2619605), anti-p-eIF2α (S51) (D9G8) (rabbit, Cell Signaling, 3398, 1:300, AB_2096481), anti-E-cadherin (24E10) (rabbit, Cell Signaling, 3195, 1:300, AB_2291471), anti-Ly6G (rat, BioLegend, 127601, 1:100, AB_1089179), anti-HIF1α (rabbit, Novus, NB100-479, 1:300, AB_10000633), anti-CGRP (rabbit, Cell Signaling, 14959, 1:300, AB_2798662).

The following Alexa-conjugated donkey secondary antibodies (Jackson ImmunoResearch) were used at 1:300 dilution of a 1 mg ml^{-1} stock solution (in 50% glycerol): AlexaFluor 488 anti-rabbit IgG (711-545-152), AlexaFluor 488 anti-chicken IgY (703-545-155), AlexaFluor 594 anti-rabbit IgG (711-585-152), AlexaFluor 594 anti-mouse IgG (711-585-150), AlexaFluor 594 anti-rat IgG (712-585-153), AlexaFluor 647 anti-rabbit IgG (711-605-152) and AlexaFluor 647 anti-mouse IgG (715-605-151).

Mouse intestinal tissue preparation

Mouse intestines were prepared according to the Swiss-roll methodology that allows efficient analysis of epithelial morphology[72,73]. In brief, mouse intestines were isolated from freshly euthanized mice and placed

immediately in ice-cold PBS. Intestines were carefully handled with forceps and flushed multiple times using a 20 ml syringe to clear stool and any remaining debris. At this stage, the colon and small intestines were cut and handled separately. A 1 ml glass pipette was inserted into the tissue and carefully laid on a large piece of Whatman filter paper. A sharp blade was used to cut intestines longitudinally down the length of the pipette which was then lightly rolled sideways to flatten the tissue on filter paper. The flattened tissue was subsequently rolled on a Gmark cotton swab stick and immersed in ice cold 4% PFA for overnight fixation at 4 °C. The next day, intestines were washed three times with ice-cold PBS and soaked in 15% sucrose/PBS followed by 30% sucrose/PBS solution each overnight to preserve tissue morphology. Tissues were subsequently embedded in OCT, sectioned and stained as described above.

Motor and sensory behavioural testing

Studies of behavioural recovery of mice after SCI with *Ahr* cKO were conducted randomized and blinded. Other behavioural data collection experiments were not randomized, and investigators were not blinded. All animals were acclimatized to the isolated procedure room for 30 min before testing. For motor function recovery testing after sciatic nerve injury, hindpaw prints were collected before and after sciatic nerve crush injury. Hindpaws were pressed on an ink pad and mice were then allowed to walk on white paper to collect the prints. The SFI was calculated by measuring dimensions of the paw prints[74], using the following formula: SFI = −38.3 × (experimental print length − normal print length)/normal print length + 109.5 × (experimental total spread − normal total spread)/normal total spread + 13.3 × (experimental intermediate toes − normal intermediate toes)/normal intermediate toes − 8.8. For analysis of sensory functional recovery, von Frey filament tests were performed[75]. The plantar surface of the hindpaw was pricked with a series of fine filaments and the mechanical threshold that evoked a withdrawal reflex was recorded. For ladder walking test, regular rungs were spaced evenly at 1 cm and irregular rungs were arranged in a pseudorandom pattern with variable spacing (1–3 cm). Mice were allowed to walk the length of the ladder while a video was recorded. Each hindlimb step was categorized as correct placement, partial slip or full slip. The number of errors was normalized to the total number of steps to calculate an error rate for each animal. To conduct open-field BMS testing, mice were placed in an open field for 5 min to allow two observers to evaluate freely roaming mice by assessing the following parameters: ankle movements, stepping pattern, coordination, paw placement, trunk stability and tail movement. The mice were scored according to the BMS scoring system[64,76,77]. Mice were tested before injury (baseline), 2 days after injury and then weekly thereafter. Mice with BMS scores above 5 at 2 days after injury (incomplete injuries) or any mouse that died prematurely before the end of the study were excluded from analysis.

Image analysis

Fluorescence images of mouse DRG neurons, human induced neurons, cortical neurons, sciatic nerves, DRGs, spinal cords and intestinal tissues were acquired using the Zeiss Axioscope microscope equipped with an AxioCam MRm camera and controlled by AxioVision Rel. 4.8 or ZEN 3.6 (Blue edition) software. Where indicated, confocal imaging of mouse footpad tissue and DRG neurons was performed using the Zeiss LSM 780 confocal microscope with ZEN 2012 software. Quantifications were performed using Fiji/ImageJ (v.2.3.0/1.53q) as previously described[5].

The length of the longest neurite of each neurite-bearing neuron (neurite longer than the diameter of its soma) was measured using the Simple Neurite Tracer (SNT v.4.0.3). The percentage of neurite-bearing neurons was calculated by counting neurons with neurites longer than the diameter of soma relative to total neurons. Quantification of cytoplasmic to nuclear shuttling was performed by measuring the nuclear signal relative to total signal for each individual neuron for both cultured cells and DRGs. For DRG tissue image analysis, the threshold function was used to quantify the percentage area per section or cell number relative to total determined by DAPI staining. Quantification of cell markers in intestines was conducted by manual cell counting in multiple villi per section.

Adult mouse cortical neuron images were quantified using the Neurite Outgrowth Analysis Module in MetaXpress 6 software (Molecular Devices). The number of valid neurons was determined by quantifying the number of $TUBB3^+DAPI^+$ cells in a well with ≥10 µm of total neurite outgrowth. Total neurite outgrowth was determined by dividing the length of all neurites in a well by the number of valid neurons in that respective well.

To establish a regeneration index of injured sciatic nerves, tiled images were merged using Photoshop CC 2019 or Paint (v.11.2511.291.0). The SCG10 fluorescence intensity was measured along the length of the nerve using ImageJ. A rectangular region of interest containing the lesion site and adjacent proximal and distal areas was selected to generate a plot profile. The position with maximal SCG10 profile intensity was used to normalize the regeneration index and the position with minimal intensity was used for subtraction of background value. The most-distal SCG10 fluorescence intensity above background was used to determine maximal axonal length. For skin reinnervation analysis, maximal-intensity projections of 400 mm *z*-stack images were used for quantification of percentage of $PGP9.5^+$ puncta normalized to the area of footpad using Fiji/ImageJ. Data organization and figure preparation were performed using Microsoft Office, PowerPoint and Excel (v.2601).

RNA-seq analysis

Ipsilateral and contralateral sciatic DRGs were collected from control or Ahr^{cKO} mice at 1 d.p.i. after sciatic nerve transection. For next-generation sequencing, RNA was isolated from DRG tissues using the Qiagen RNeasy plus mini kit, and cDNA libraries were sequenced on the Illumina NovaSeq platform (Psomagen). Preprocessing, quality control and alignment of FASTQ files was performed using the NGS-Data-Charmer pipeline. Trim-Galore tool (v.0.6.5)[78] was used for adaptor trimming and alignment to the mouse mm10 genome assembly was performed with Bowtie2 (v.2.4.1)[79]. The 'rmdup' module of SAMtools (v.1.10)[80] was used to remove duplicated read pairs. FeatureCounts was used to obtain a gene expression matrix, using the parameters '--fraction -t gene' on the GENCODE annotation (vM25). For gene filtering, genes with >5 read counts and in >5 samples were retained before performing differential gene expression analysis with DESeq2. For visualization of genome-wide RNA-seq read distribution, aligned BAM files were further processed into BigWig file format and visualized in the Integrative Genomics Viewer (IGV)[81] for inspection of *Ahr* exon read coverage.

Bioinformatics

TF interaction networks were generated using STRING database[82], with the default setting of medium confidence. AhR and HIF1α putative target genes were identified using ChIP-X Enrichment Analysis with ChEA3[83]. Heat maps, volcano plots, bubble plots, bar graphs, box plots and violin plots were generated with FLASKi[84], OriginPro 2019/2020b and GraphPad Prism v.9/v.10. GSEA was performed using the GSEA v.4.3.2 software provided by the Broad Institute[85], using the non-preranked whole DRG genome and Hallmark_MSigDB gene sets. Pathway enrichment in gene sets was performed with Enrichr[86,87] and Ingenuity Pathway Analysis Qiagen knowledge database (IPA; v.153384343)[88] with the whole list of expressed genes as background. For Enrichr, pathways with adjusted $P < 0.05$ (Fisher's exact test, Benjamini–Hochberg correction) were retained and ranked by combined score. Pathways shown were subsequently curated for biological relevance to the study context. Identification of experimentally validated promoter motifs was conducted using the Eukaryotic Promoter Database platform[89]. RSS analysis of *Ahr*-cKO-dependent PL-DEGs was calculated as $\Delta\log_2[FC] = \log_2[FC\ (cKO)] - \log_2[FC\ (control)]$. Adjusted *P* values (Benjamini–Hochberg FDR correction) were derived from the

original differential expression analyses used to define differentially expressed genes ($|\Delta\log_2[FC]| \geq 0.3$, adjusted $P < 0.05$) before calculation of RSSs. The RSS itself represents a derived comparative metric and was not subjected to additional statistical testing.

Statistical analysis

For each dataset, the Shapiro–Wilk test was performed to test data normality ($P > 0.05$ determined as parametric and $P \leq 0.05$ determined as nonparametric). For parametric data, unpaired two-tailed Student's *t*-tests were used for comparisons between two groups, one-way analysis of variance (ANOVA), Holm–Šidák multiple-test correction was used for comparisons of three groups, and two-way ANOVA followed by Bonferroni's multiple-comparison test was used for multiple-group comparisons. For nonparametric data, Mann–Whitney two-tailed *t*-tests were used for comparisons between two groups and Kruskal–Wallis test with Dunn's multiple-test correction for comparisons between multiple groups. All statistical analyses were performed with GraphPad Prism v.9 or 10. The GraphPad Prism setting NEJM (New England Journal of Medicine) for reporting of *P* values was applied. $P \leq 0.05$ was considered to be statistically significant. Statistical significance for pathway enrichment was evaluated using GSEA with permutation-derived nominal *P* values and FDR *q* values as recommended by the Broad Institute guidelines.

Reporting summary

Further information on research design is available in the Nature Portfolio Reporting Summary linked to this article.

Data availability

RNA-seq data generated in this study (Ahr^{cKO} dataset) have been deposited in the NCBI Gene Expression Omnibus (GEO) under accession number GSE307639 (mm10 mouse genome assembly). Publicly available resources used for analysis include the STRING database (https://string-db.org), GREAT v.4.0 (http://great.stanford.edu/public/html/index.php), the Eukaryotic Promoter Database (EPD; https://epd.epfl.ch/index.php), the conditioned DRG neuron scRNA-seq database PainSeq (https://painseq.shinyapps.io/publish/) and the Mouse Brain Atlas for nervous system expression analysis of *Ahr* (http://mousebrain.org). IPA (Qiagen) was accessed under an institutional license held by the Icahn School of Medicine at Mount Sinai. Source data are provided with this paper.

Code availability

An R script of the analysis of differentially expressed genes is provided in the Supplementary Information files. Other RNA-seq analyses were performed using established and widely adopted R workflows and publicly available bioinformatics tools as stated in the Methods. Additional details are available from the corresponding author on request.

54. Heimer-McGinn, V. & Young, P. Efficient inducible Pan-neuronal cre-mediated recombination in SLICK-H transgenic mice. *Genesis* **49**, 942–949 (2011).
55. Young, P. et al. Single-neuron labeling with inducible Cre-mediated knockout in transgenic mice. *Nat. Neurosci.* **11**, 721–728 (2008).
56. Tronche, F. et al. Disruption of the glucocorticoid receptor gene in the nervous system results in reduced anxiety. *Nat. Genet.* **23**, 99–103 (1999).
57. Walisser, J. A., Glover, E., Pande, K., Liss, A. L. & Bradfield, C. A. Aryl hydrocarbon receptor-dependent liver development and hepatotoxicity are mediated by different cell types. *Proc. Natl Acad. Sci. USA* **102**, 17858–17863 (2005).
58. Mo, A. et al. Epigenomic signatures of neuronal diversity in the mammalian brain. *Neuron* **86**, 1369–1384 (2015).
59. Tomita, S., Sinal, C. J., Yim, S. H. & Gonzalez, F. J. Conditional disruption of the aryl hydrocarbon receptor nuclear translocator (Arnt) gene leads to loss of target gene induction by the aryl hydrocarbon receptor and hypoxia-inducible factor 1α. *Mol. Endocrinol.* **14**, 1674–1681 (2000).
60. Sun, L. Recent advances in the development of AHR antagonists in immuno-oncology. *RSC Med. Chem.* **12**, 902–914 (2021).
61. Narita, T. et al. Identification of a novel small molecule HIF-1α translation inhibitor. *Clin. Cancer Res.* **15**, 6128–6136 (2009).
62. Sidrauski, C. et al. Pharmacological brake-release of mRNA translation enhances cognitive memory. *eLife* **2**, e00498 (2013).
63. Obata, Y. et al. Neuronal programming by microbiota regulates intestinal physiology. *Nature* **578**, 284–289 (2020).
64. Ghnenis, A. B. et al. Evaluation of the cardiometabolic disorders after spinal cord injury in mice. *Biology* **11**, 495 (2022).
65. Zhou, X. et al. Microglia and macrophages promote corralling, wound compaction and recovery after spinal cord injury via Plexin-B2. *Nat. Neurosci.* **23**, 337–350 (2020).
66. Kuboyama, T. et al. HDAC3 inhibition ameliorates spinal cord injury by immunomodulation. *Sci. Rep.* **7**, 8641 (2017).
67. Halawani, D. et al. Identification of caspase-6-mediated processing of the valosin containing protein (p97) in Alzheimer's disease: a novel link to dysfunction in ubiquitin proteasome system-mediated protein degradation. *J. Neurosci.* **30**, 6132–6142 (2010).
68. Bowles, K. R., Tcw, J., Qian, L., Jadow, B. M. & Goate, A. M. Reduced variability of neural progenitor cells and improved purity of neuronal cultures using magnetic activated cell sorting. *PLoS ONE* **14**, e0213374 (2019).
69. Frey, E. et al. An in vitro assay to study induction of the regenerative state in sensory neurons. *Exp. Neurol.* **263**, 350–363 (2015).
70. Goodman, C. A. et al. Novel insights into the regulation of skeletal muscle protein synthesis as revealed by a new nonradioactive in vivo technique. *FASEB J.* **25**, 1028–1039 (2011).
71. Goodman, C. A. & Hornberger, T. A. Measuring protein synthesis with SUnSET: a valid alternative to traditional techniques? *Exerc. Sport Sci. Rev.* **41**, 107–115 (2013).
72. Bialkowska, A. B., Ghaleb, A. M., Nandan, M. O. & Yang, V. W. Improved Swiss-rolling technique for intestinal tissue preparation for immunohistochemical and immunofluorescent analyses. *J. Vis. Exp.* https://doi.org/10.3791/54161 (2016).
73. Yoneda, M., Molinolo, A. A., Ward, J. M., Kimura, S. & Goodlad, R. A. A simple device to rapidly prepare whole mounts of the mouse intestine. *J. Vis. Exp.* https://doi.org/10.3791/53042 (2015).
74. Marcolino, A. M. et al. Assessment of functional recovery of sciatic nerve in rats submitted to low-level laser therapy with different fluences. An experimental study: laser in functional recovery in rats. *J. Hand Microsurg.* **5**, 49–53 (2013).
75. Li, Y. et al. Macrophages facilitate peripheral nerve regeneration by organizing regeneration tracks through Plexin-B2. *Genes Dev.* **36**, 133–148 (2022).
76. Basso, D. M. et al. Basso Mouse Scale for locomotion detects differences in recovery after spinal cord injury in five common mouse strains. *J. Neurotrauma* **23**, 635–659 (2006).
77. Hook, M. A. et al. Osteopenia in a mouse model of spinal cord injury: effects of age, sex and motor function. *Biology* **11**, 189 (2022).
78. Martin, M. Cutadapt removes adapter sequences from high-throughput sequencing reads. *EMBnet J.* **17**, 3 (2011).
79. Langmead, B. & Salzberg, S. L. Fast gapped-read alignment with Bowtie 2. *Nat. Methods* **9**, 357–359 (2012).
80. Danecek, P. et al. Twelve years of SAMtools and BCFtools. *Gigascience* **10**, giab008 (2021).
81. Robinson, J. T. et al. Integrative Genomics Viewer. *Nat. Biotechnol.* **29**, 24–26 (2011).
82. Szklarczyk, D. et al. The STRING database in 2021: customizable protein-protein networks, and functional characterization of user-uploaded gene/measurement sets. *Nucleic Acids Res.* **49**, D605–D612 (2021).
83. Keenan, A. B. et al. ChEA3: transcription factor enrichment analysis by orthogonal omics integration. *Nucleic Acids Res.* **47**, W212–W224 (2019).
84. Iqbal, A. et al. Flaski (3.12.2). *Zenodo* https://doi.org/10.5281/zenodo.7329954 (2022).
85. Subramanian, A. et al. Gene set enrichment analysis: a knowledge-based approach for interpreting genome-wide expression profiles. *Proc. Natl Acad. Sci. USA* **102**, 15545–15550 (2005).
86. Chen, E. Y. et al. Enrichr: interactive and collaborative HTML5 gene list enrichment analysis tool. *BMC Bioinform.* **14**, 128 (2013).
87. Kuleshov, M. V. et al. Enrichr: a comprehensive gene set enrichment analysis web server 2016 update. *Nucleic Acids Res.* **44**, W90–W97 (2016).
88. Krämer, A., Green, J., Pollard, J. & Tugendreich, S. Causal analysis approaches in Ingenuity Pathway Analysis. *Bioinformatics* **30**, 523–530 (2014).
89. Dreos, R., Ambrosini, G., Périer, R. C. & Bucher, P. The Eukaryotic Promoter Database: expansion of EPDnew and new promoter analysis tools. *Nucleic Acids Res.* **43**, D92–D96 (2015).

Acknowledgements We thank all of the members of the Zou laboratory for help and suggestions; and F. Gonzalez for providing the *Arnt-flox* mouse line. This work was supported by grants from the NIH (R01 NS127442), the New York State SCIRB (Spinal Cord Injury Research Board) (DOH01 C38330GG, C41211GM) and the Neilsen Foundation (890112) to H.Z., and by NIH R21NS131834 and R01NS128101 to C.G.G. Y.W. was partly supported by a scholarship fund from Xi'an Jiaotong University. D. Halperin was supported by a fellowship of the Wings for Life Foundation.

Author contributions Conceptualization: D. Halawani, Y.W., R.H.F. and H.Z. Data acquisition: D. Halawani, Y.W., J.L., D. Halperin, H.N. and A.S. Data analysis: D. Halawani, Y.W., A.S., C.G.G., R.H.F. and H.Z. Bioinformatic analysis: M.E., D. Halawani, Y.W., A.R. and L.S. Manuscript writing: D. Halawani, Y.W., R.H.F. and H.Z.

Competing interests The authors declare no competing interests.

Additional information

Supplementary information The online version contains supplementary material available at https://doi.org/10.1038/s41586-026-10295-z.

Correspondence and requests for materials should be addressed to Hongyan Zou.

Peer review information *Nature* thanks the anonymous reviewer(s) for their contribution to the peer review of this work.

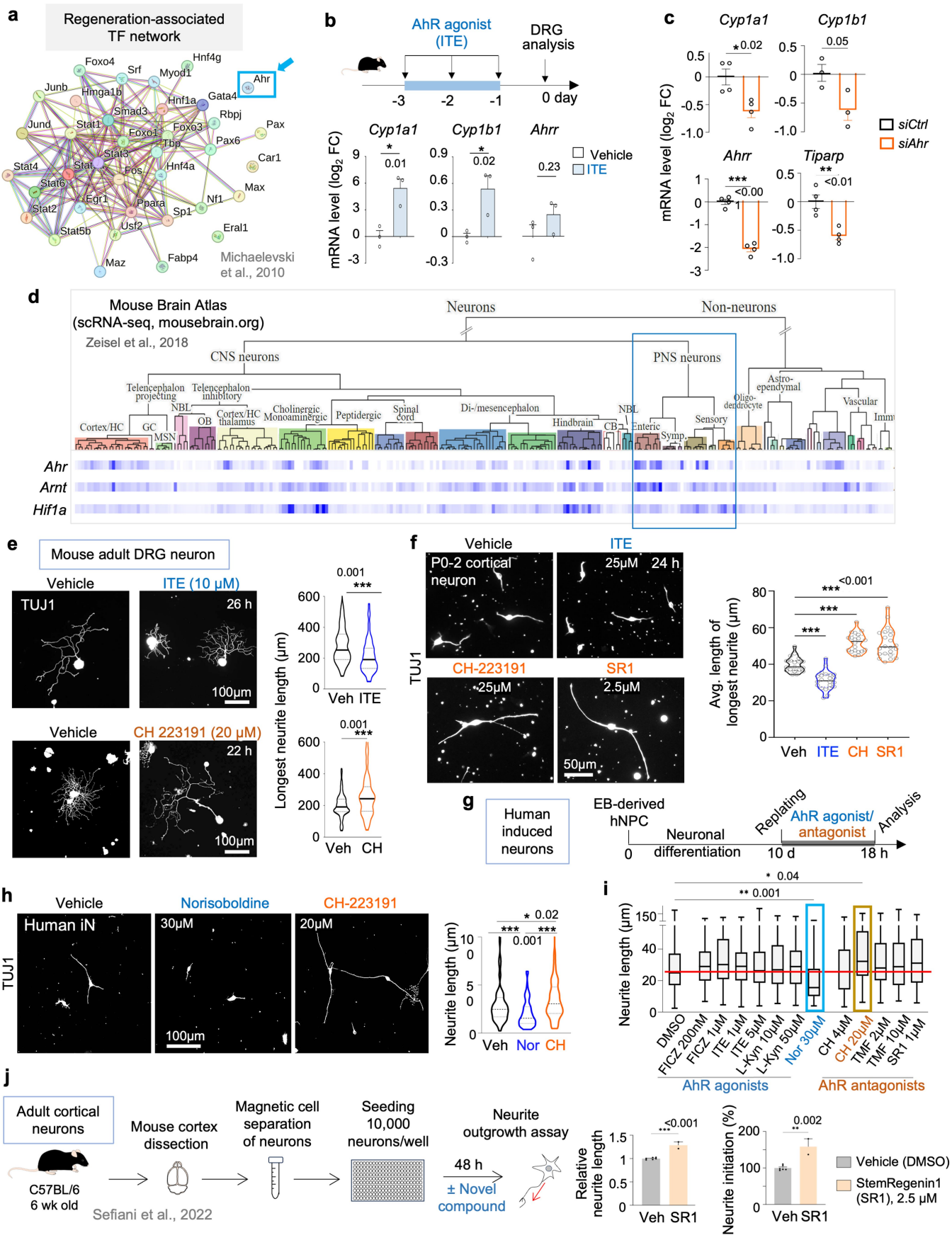

Extended Data Fig. 1 | See next page for caption.

Extended Data Fig. 1 | AhR inhibition enhances neurite outgrowth across PNS and CNS neurons. a, STRING analysis of protein-protein interaction network of transcription factors (TFs) induced after conditioning lesion of DRG. **b**, qRT-PCR of AhR target genes in DRGs from adult mice treated with ITE (10 mg/kg i.p.) or vehicle. n = 3 DRGs from 3 mice. Unpaired two-tailed *t*-test. **c**, qRT-PCR shows downregulation of AhR target genes 48 h after siRNA knockdown of *Ahr*. n = 3 cultures for *Cyp1b1*, n = 4 for the rest. Unpaired two-tailed *t*-test. **d**, Heatmap of *Ahr*, *Arnt*, and *Hif1a* expression across cell types of the mouse nervous system. **e**, IF of adult primary DRG neurons for $TUJ1^+$ neurites. ITE treatment: n = 74 neurons (vehicle), 100 (ITE), from 2 mice. CH: n = 120 neurons (vehicle), 188 (CH), from 2 mice. Median and quartiles shown. Mann-Whitney two-tailed test. **f**, Cultures of neonatal cortical neurons. Mean longest neurite from n = 19 random fields for vehicle, 22 for ITE, 20 for CH, and 22 for SR1 across independent cultures from 2 mice. Violin plots show median and quartiles. One-way ANOVA with Dunnett's correction. **g-i**, Paradigm of induced neurons (iNs) derivation and AhR agonist/antagonist treatment (**g**). IF images show Norisoboldine (Nor) treatment reduced neurite length, whereas CH-223191 (CH) enhanced outgrowth (**h**). n = 83 (Veh), 90 (Nor), and 106 (CH) cells. One-way ANOVA with Dunnett's correction. Violin plots show median and quartiles. Box plots of neurite length (median and quartiles) after 18 hr of treatment (**i**). n = 70 –116 neurons. Highlighted conditions (Nor, CH) correspond to (**h**). Kruskal-Wallis test with Dunn's correction; only significant *P* values shown. **j**, Left, schematic of high-throughput screen for neurite growth-promoting compounds in adult cortical neurons (Sefiani et al.[25]). Right, quantification of AhR antagonist SR1 effects on neurite growth. Each data point represents mean of >150 neurons (with neurites ≥ 10 µm) from a single well. n = 2–6 wells per group. Mean ± s.e.m. Unpaired two-tailed Student's *t*-test. Data are mean ± s.e.m.

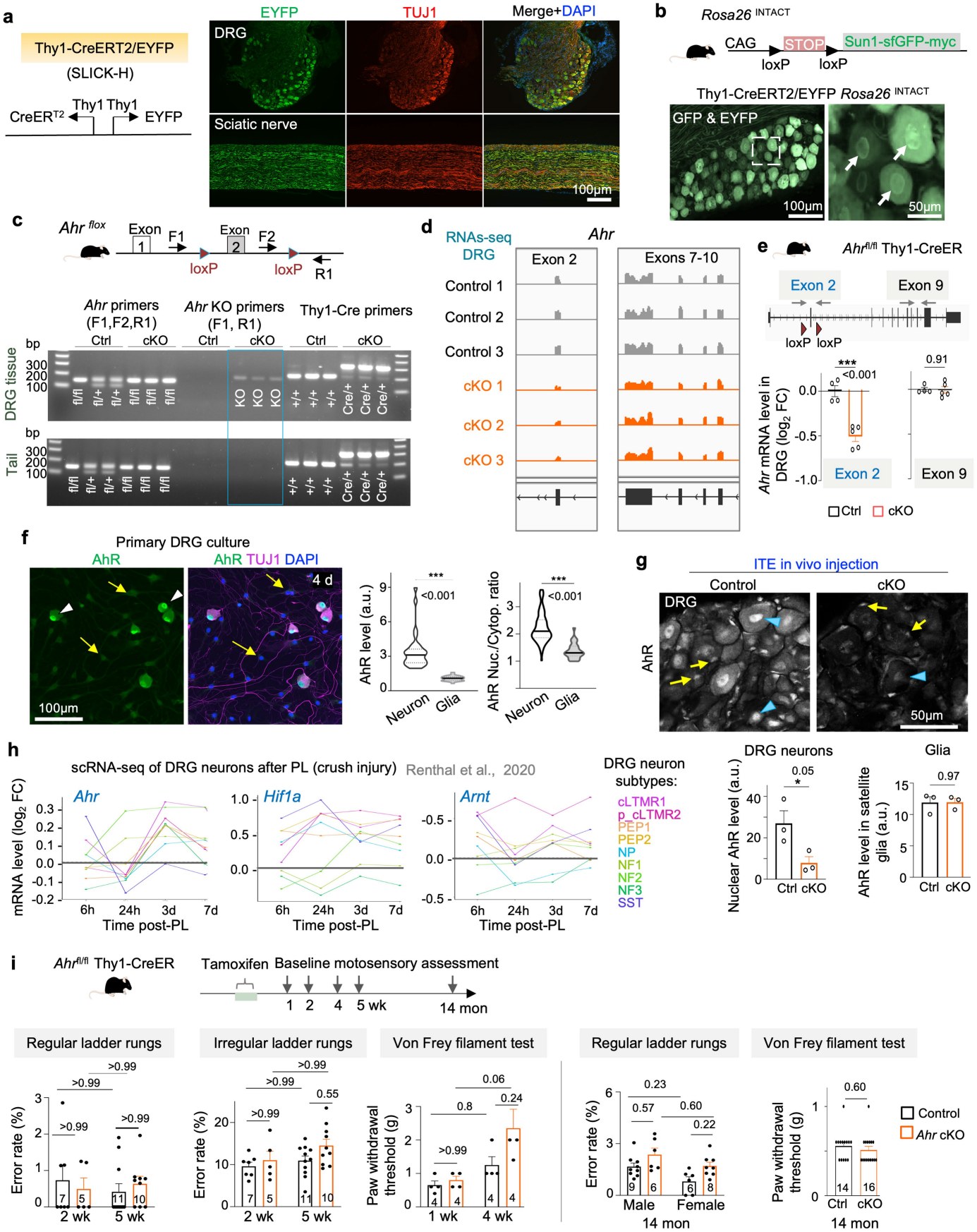

Extended Data Fig. 2 | See next page for caption.

Extended Data Fig. 2 | Validation of neuronal *Ahr* cKO mice and normal baseline motosensory performance. a, Diagram of the SLICK-H transgenic line expressing tamoxifen-inducible CreERT2 and EYFP under bidirectional Thy1 promoter. IF images of DRG and sciatic nerve show pan-neuronal (TUJ1^{+}) EYFP expression (anti-GFP IF). DAPI, nuclear counterstain. **b**, Rosa26 INTACT (isolation of nuclei tagged in specific cell types) reporter allele. IF of DRG section reveals cytoplasmic GFP from Thy1-CreERT2/EYFP allele and nuclear membrane GFP from INTACT/Sun1-GFP reporter (arrows). **c**, *Ahr* floxed allele with loxP sites flanking exon 2 and genotyping primers indicated. PCR genotyping of $Ahr^{fl/fl}$ Thy1-CreERT2/EYFP mice confirmed excision of *Ahr* exon 2 in DRG but not tail at 2 weeks after tamoxifen (100 mg/kg i.p. x 5 d). **d**, RNA-seq read tracks (3 examples/genotype) show reduced *Ahr* exon 2, but no change in downstream exons 7–10 in DRGs of *Ahr* cKO mice compared to controls. **e**, *Ahr* cKO allele with loxP sites flanking exon 2 and qRT-PCR primers covering exons 2 and 9. Reduced *Ahr* transcript containing exon 2 in sciatic DRGs from *Ahr* cKO mice (n = 5) compared to controls (n = 4). One-way ANOVA with Dunnett's correction. **f**, IF of primary DRG cultures shows higher nuclear AhR signals in TUJ1^{+} neurons (arrowheads) compared to glia (yellow arrows). For AhR intensity, n = 30 cells; nuclear/cytoplasmic AhR ratio, n = 100 neurons and 30 glia from 3 cultures. Violin plots show median and quartiles. Unpaired two-tailed t-test. **g**, DRGs from ITE treated mice show high nuclear levels of AhR in neurons, which was ablated in *Ahr* cKO. No significant changes were observed in glial AhR levels (yellow arrows), which displayed lower levels than neurons. n = 3 L5 DRGs/condition. Unpaired two-tailed *t*-test. **h**, Expression of *Ahr*, *Hif1a*, and *Arnt* across DRG neuron subtypes after PL. **i**, Top, timeline of motosensory performance assessment after neuronal *Ahr* cKO at baseline without injury. Sample sizes are indicated in graphs. Two-way ANOVA with Bonferroni correction; Mann-Whitney test for von Frey assay. Data are mean ± s.e.m.

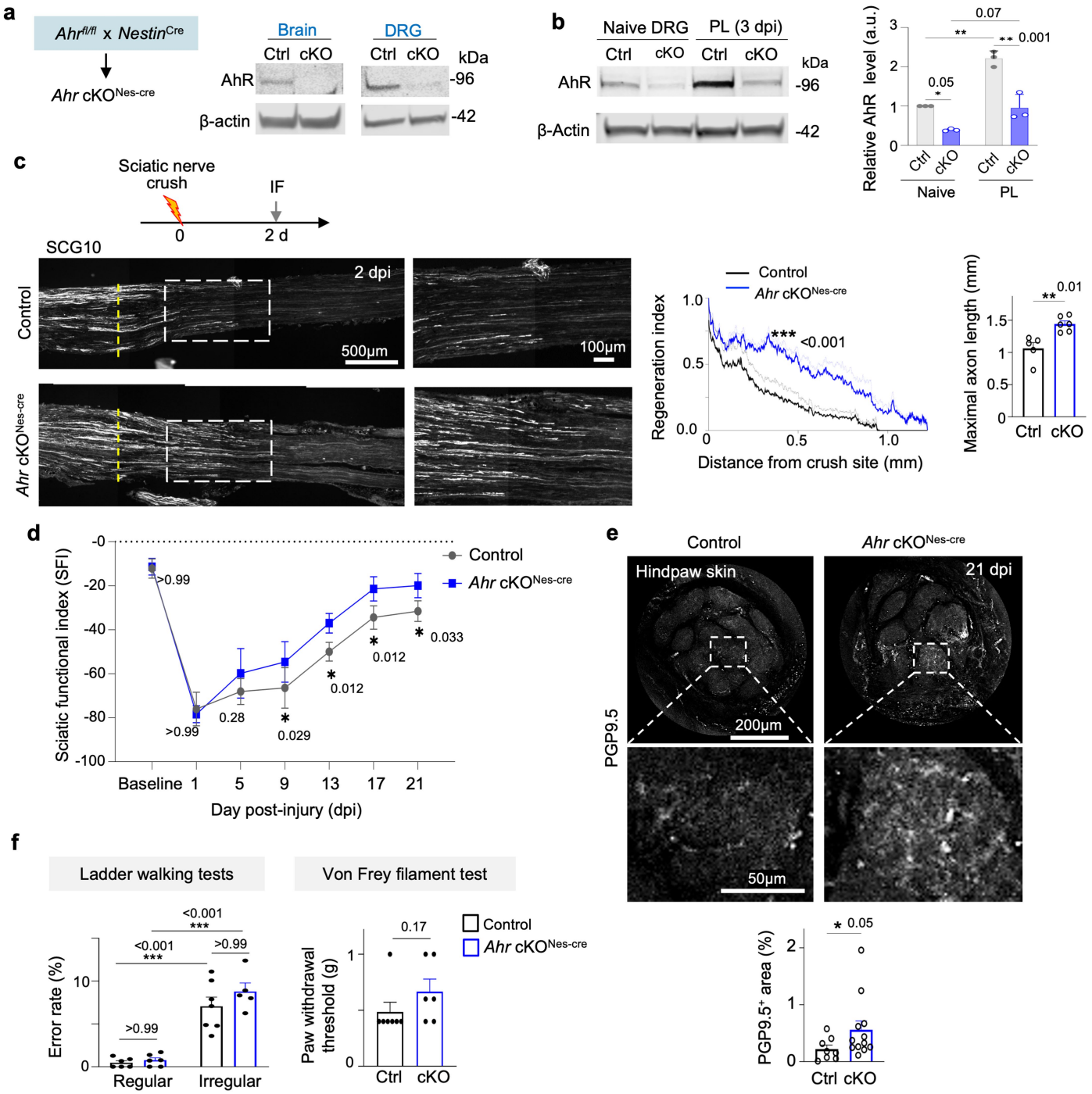

Extended Data Fig. 3 | *Ahr* cKO (Nestin-Cre) accelerates axon regeneration after sciatic nerve injury. a, Immunoblots show reduction of AhR protein in brain and DRG from *Ahr* cKO (Nestin-Cre) mice. β-actin, loading control. **b**, Immunoblots and quantification of AhR protein in naive and conditioned DRG (3 dpi after PL) from *Ahr* cKO (Nestin-Cre) and control mice. n = 3 samples (each from pooled L4-L6 DRGs) from 3 mice per genotype. Two-way ANOVA with Bonferroni correction. **c**, IF images of SCG10$^+$ axons traversing lesion centre (dashed vertical line) at 2 dpi in Nestin-Cre *Ahr* cKO and controls. Right, quantification of regeneration index and maximal axon length. n = 5 control, n = 6 cKO mice. Regeneration index: two-way ANOVA with Bonferroni correction. Maximal axon length: unpaired two-tailed Student's t-test. **d**, Sciatic functional index (SFI) measurements show improved motor recovery in Nestin-Cre cKO mice. n = 5 per group. Two-way ANOVA with Bonferroni correction. **e**, Whole mount IF for PGP9.5 shows enhanced epidermal re-innervation in cKO mice at 21 dpi. Images represent maximal-intensity projections of ~400 μm footpad sections spanning top, middle, and lower epidermis. Quantification of PGP9.5$^+$ area from two footpads per mouse. n = 4 control, n = 6 cKO mice. Unpaired two-tailed *t*-test. **f**, Baseline motosensory tests. n = 7 control, n = 6 cKO mice. Ladder walking: two-way ANOVA with Bonferroni correction. Von Frey assay: Mann-Whitney two-tailed test. Data are mean ± s.e.m.

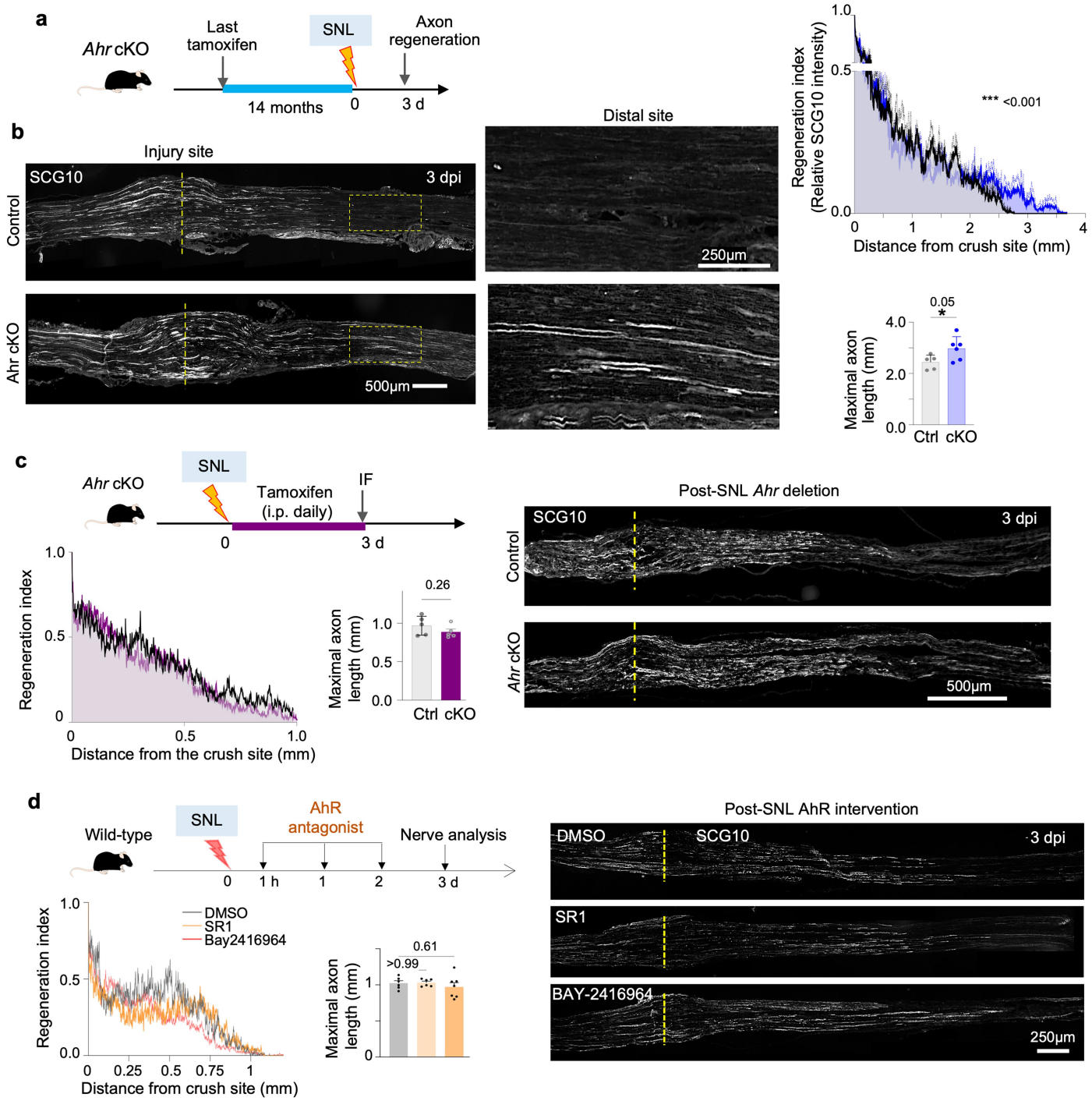

Extended Data Fig. 4 | Neuronal *Ahr* deletion enhances regeneration in older mice but no effect of AhR inhibition post-injury. a, b, Long-term neuronal *Ahr* cKO paradigm (**a**). Tamoxifen (100 mg/kg i.p., daily x 5) was administered 14 months before sciatic nerve crush. IF of SCG10$^+$ axons at 3 dpi shows enhanced regeneration in cKO mice compared to controls (**b**). Regeneration index: two-way ANOVA with Bonferroni correction; maximal axon length distal to lesion centre: n = 5 control, n = 6 cKO; unpaired two-tailed *t*-test. **c**, Post-injury *Ahr* cKO paradigm. Tamoxifen (100 mg/kg i.p., daily x 3) was administered immediately after sciatic nerve crush. At 3 dpi, SCG10$^+$ axon regeneration was comparable between cKO and control mice (n = 5 per group). Regeneration index: two-way ANOVA with Bonferroni correction; maximal axon length distal to lesion centre: unpaired two-tailed *t*-test. **d**, Post-injury AhR antagonist treatment. SR1 (25 mg/kg), BAY-2416964 (25 mg/kg), or vehicle (DMSO) were administered daily x 3 immediately after sciatic nerve crush. At 3 dpi, IF of SCG10$^+$ axons showed no significant differences between groups. n = 6 mice (DMSO, SR1), n = 7 (BAY). One-way ANOVA with Dunnett's correction. Data are mean ± s.e.m.

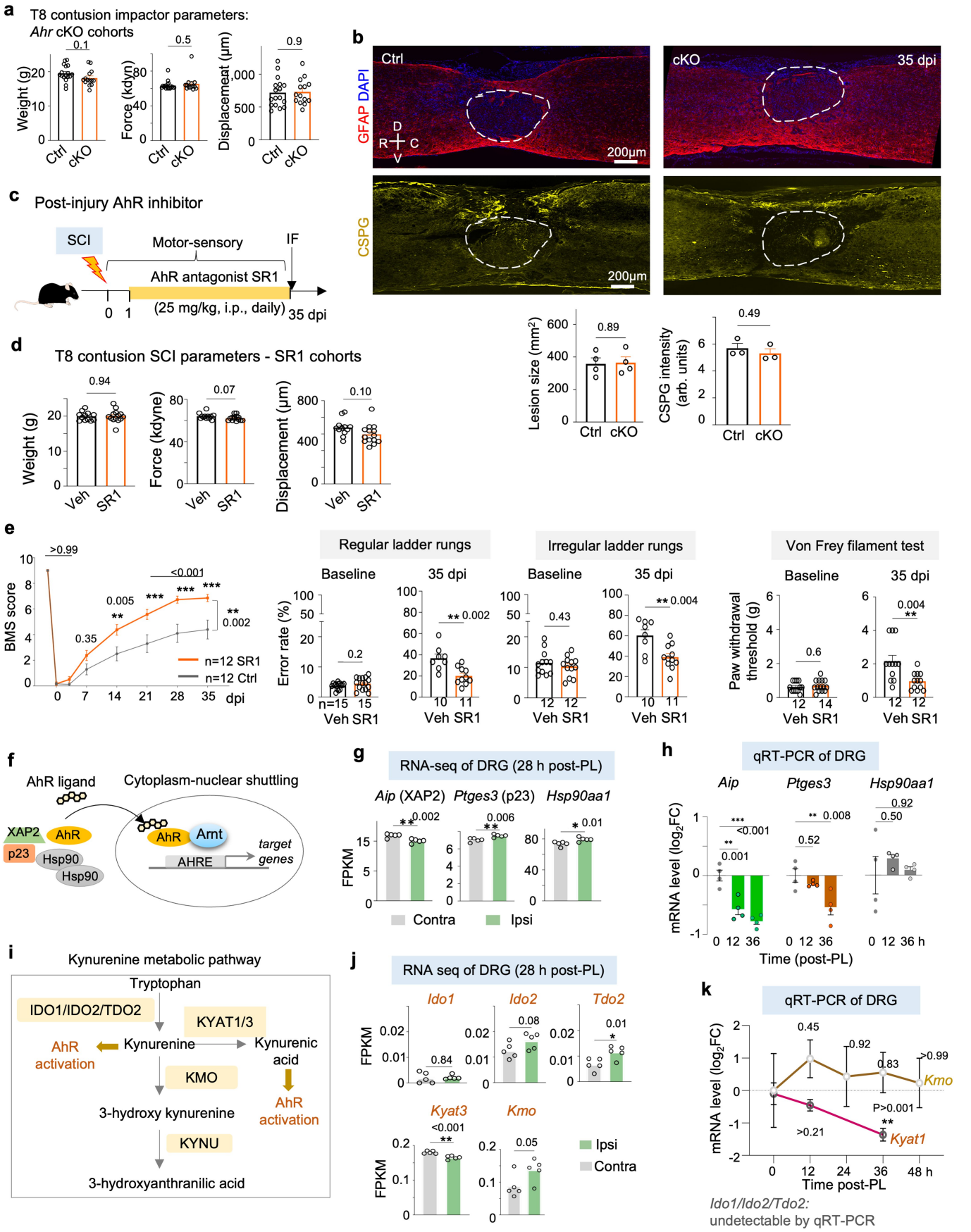

Extended Data Fig. 5 | See next page for caption.

Extended Data Fig. 5 | Post-injury AhR inhibition enhances functional recovery after SCI. No major expression changes of kynurenine pathway genes after PL. a, Contusion injury parameters with impactor device. n = 17 control and 14 cKO mice. Unpaired two-tailed *t*-test. **b**, IF for reactive astrocyte marker GFAP (n = 4 mice/group) and matrix proteoglycan CSPG (antibody clone CS-56, n = 3) at 35 dpi after SCI show comparable lesion size. Unpaired two-tailed *t*-test. **c**, In vivo administration of AhR antagonist SR1 starting at 1 day post-SCI (25 mg/kg i.p., daily). **d**, Parameters of contusion injury with impactor device in SR1 (n = 14) and control (n = 12) cohorts. Mean ± s.e.m. unpaired two-tailed *t*-test. **e**, BMS scores show improved locomotor recovery with post-injury SR1 treatment after SCI. n = 12 mice/group. Two-way ANOVA with Bonferroni correction. Ladder walking and von Frey filament testing were performed at baseline and 35 dpi. Data represent mean ± s.e.m.; unpaired two-tailed *t*-test. **f**, Diagram: AhR is sequestered in cytoplasm by two Hsp90 chaperones, p23 and XAP2. Ligand binding triggers dissociation of complex and AhR nuclear translocation. **g**, mRNA reads from RNA-seq analysis of ipsi- and contralateral sciatic DRGs. n = 5 samples/condition. Unpaired two-tailed *t*-test. **h**, Time-course qRT-PCR of sciatic DRGs at 12 h and 36 h post-PL. n = 4 samples/condition. One-way ANOVA with Dunnett's correction. **i**, Overview of tryptophan metabolism/kynurenine pathway: IDO, indoleamine 2,3 dioxygenase; TDO, tryptophan-2,3-dioxygenase; KYAT1, kynurenine amino transferase1; KMO, kynurenine 3 monooxygenase; KYNU, kynureninase. **j**, mRNA reads from RNA-seq of ipsi- and contralateral sciatic DRGs. n = 5/condition. Unpaired two-tailed *t*-test. **k**, Time-course qRT-PCR of axotomized DRGs. n = 3/condition. One-way ANOVA with DEunnett's correction. Data are mean ± s.e.m.

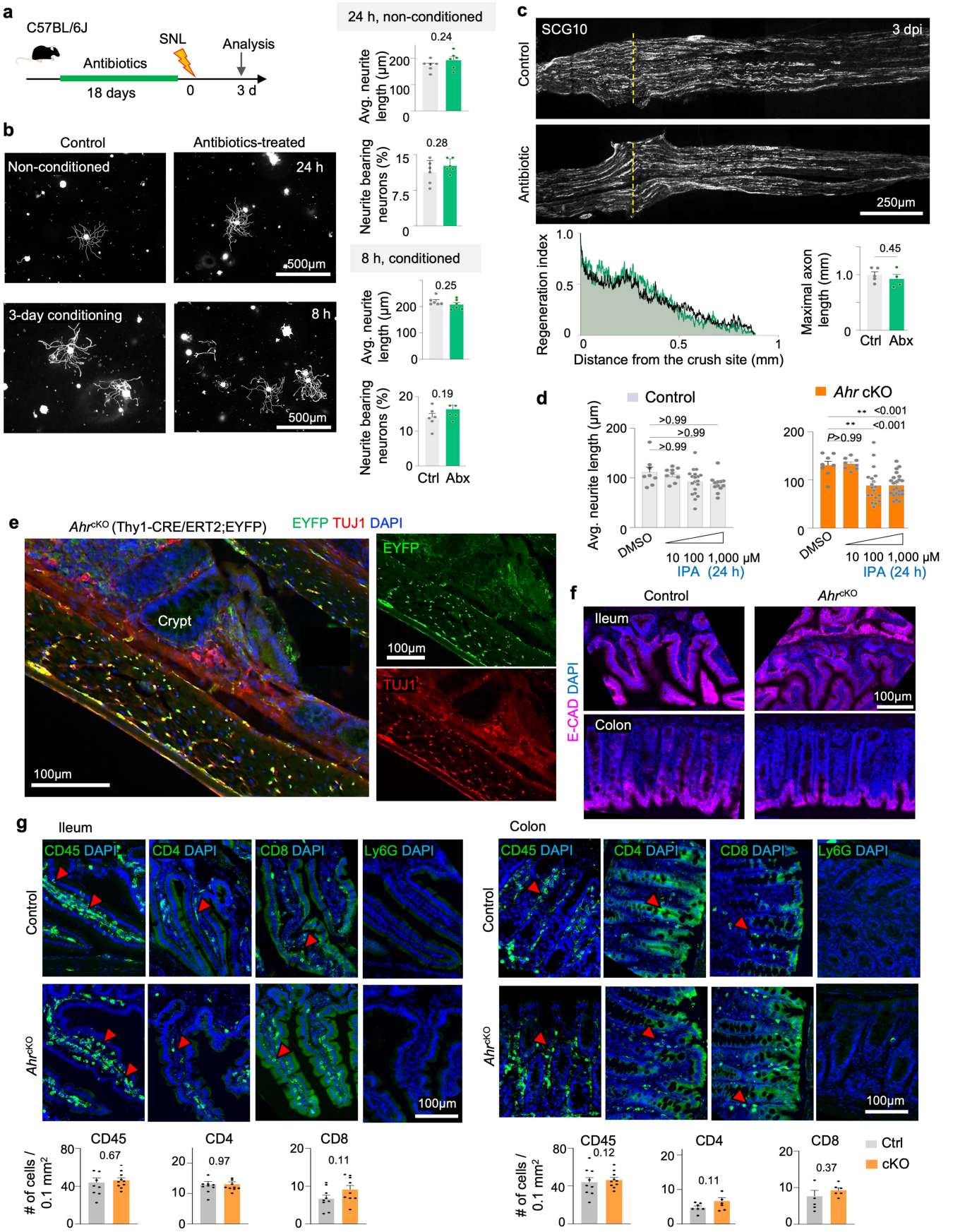

Extended Data Fig. 6 | See next page for caption.

Extended Data Fig. 6 | Gut microbiome depletion by antibiotics does not impact axon regeneration. Neuronal AhR cKO does not alter gut immune cell composition. a, Experimental design of antibiotics treatment for gut microbiome depletion. **b**, IF and quantification of neurite length of contra- and ipsilateral (conditioning) DRG neurons. n = 6 cultures per condition; each data point is mean length from 21–73 neurons. Unpaired two-tailed *t*-test. **c**, IF images of SCG10$^+$ axons at 3 dpi show comparable regeneration in control and antibiotics-treated mice. Dashed lines, lesion centre (based on highest SCG10 immunointensity). n = 5 control, n = 4 Abx-treated mice. Regeneration index: two-way ANOVA. Maximal axon length: unpaired two-tailed *t*-test. **d**, Quantifications of mean neurite length of DRG neurons treated for 24 h with increasing concentrations of indole-3-propionic acid (IPA). n = 8 to 23 datapoints per condition (each datapoint represents mean from 25 neurons), prepared from 2 mice per genotype. One-way ANOVA with Dunnett's correction. **e**, IF images of colonic myenteric plexus in Thy1-CreER/EYFP mice show EYFP expression (by IF with anti-GFP) in TUJ1$^+$ enteric neurons. **f**, Distal ileum and colon show intact epithelial architecture in *Ahr* cKO mice compared to wild-type controls. Representative images of n = 3 mice at 1 d post-sham surgery. **g**, Distal ileum and colon from sham-operated cKO and wild-type control mice were analysed for distribution of immune cell types. Data from 2–3 sections per tissue, n = 3 mice per genotype. Unpaired two-tailed *t*-test. Data are mean ± s.e.m.

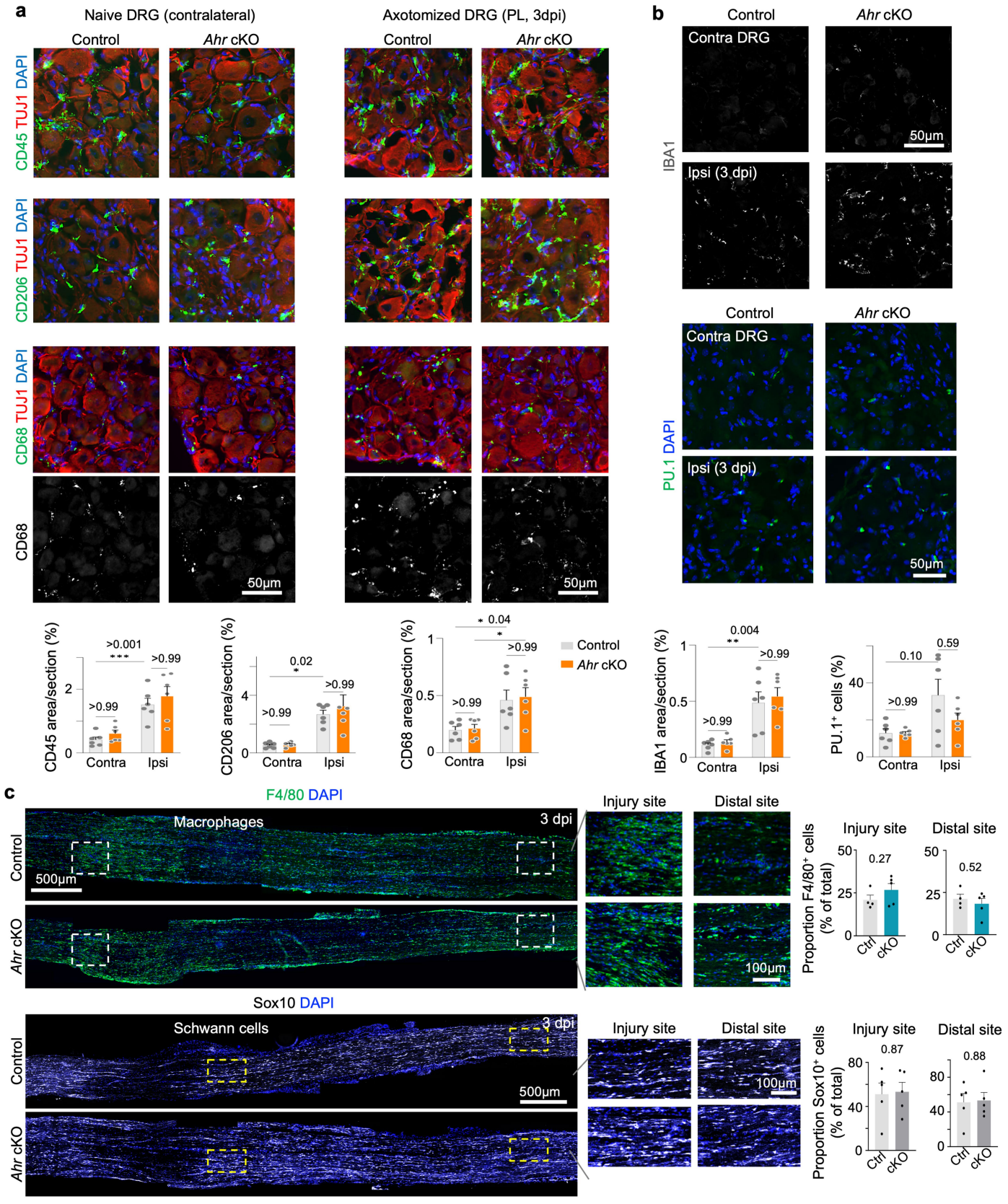

Extended Data Fig. 7 | Neuronal *Ahr* deletion does not affect immune or glial composition in axotomized DRG or injured sciatic nerve. a, b, IF images and quantifications of immune cell markers in ipsi- and contralateral DRGs at 3 dpi after PL. n = 5–6 DRGs from 2 mice per genotype. Mean ± s.e.m. Two-way ANOVA with Bonferroni correction. **c**, IF staining for F4/80$^+$ macrophages and Sox10$^+$ Schwann cells at the crush site of sciatic nerve at 3 dpi. Quantification of cell proportions at the indicated locations. n = 4 control, n = 5 cKO mice. Mean ± s.e.m. Unpaired two-tailed *t*-test.

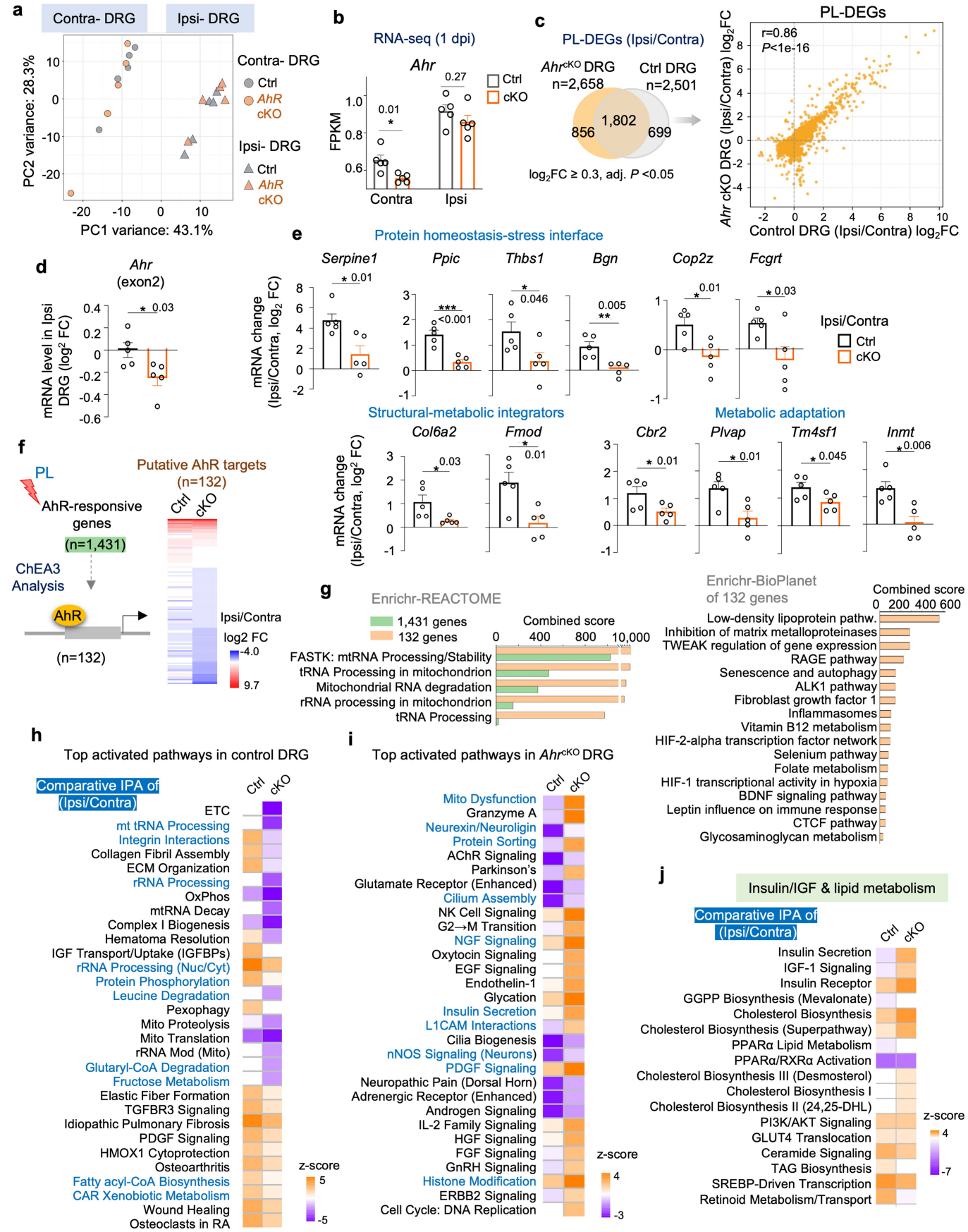

Extended Data Fig. 8 | See next page for caption.

Extended Data Fig. 8 | Neuronal *Ahr* cKO induces transcriptional shifts in DRG after peripheral lesion. a, Principal component analysis of RNA-seq samples from ipsi- and contralateral sciatic DRGs at 1 dpi (n = 5 per group) shows segregation by injury status, with only modulatory effects of *Ahr* cKO. **b**, RNA-seq analysis revealed reduced *Ahr* reads (fragments per kb transcript per million reads; FPKM) in cKO versus control DRGs. Note robust *Ahr* induction in ipsilateral DRGs after PL. n = 5 per group. Mean ± s.e.m. Unpaired two-tailed *t*-test. **c**, Venn diagram illustrates overlapping and distinct PL-associated genes (ipsi/contra) in *Ahr* cKO vs. controls. Scatter plot of $\log_2$FC values for PL-associated genes in control (x-axis) versus cKO (y-axis). **d**, qRT-PCR of ipsilateral DRG verified reduction of *Ahr* mRNA (primers spanning exon 2) in *Ahr* cKO DRGs. **e**, qRT-PCR of ipsi- vs. contralateral DRGs from control and *Ahr* cKO mice confirmed AhR-dependent response shifts of PL-induced DEGs associated with protein homeostasis and metabolic adaptation. n = 5 per group. Mean ± s.e.m. Unpaired two-tailed *t*-test. **f**, ChEA analysis of AhR-responsive genes identified 132 putative AhR target genes. Heatmap showing expression ($\log_2$FC) of PL-induced DEGs (ipsi/contra) in control versus cKO. **g**, Enrichr analysis of 1,431 AhR-responsive PL-DEGs and of the subset of 132 genes highlights shared and distinctively enriched pathways. **h, i**, Comparative IPA analyses of ipsi/contra PL-induced DEGs show the top activated pathways in control versus cKO. **j**, Comparative IPA of ipsi/contra PL-induced DEGs reveals differential pathways related to insulin/IGF and lipid metabolism in control versus cKO.

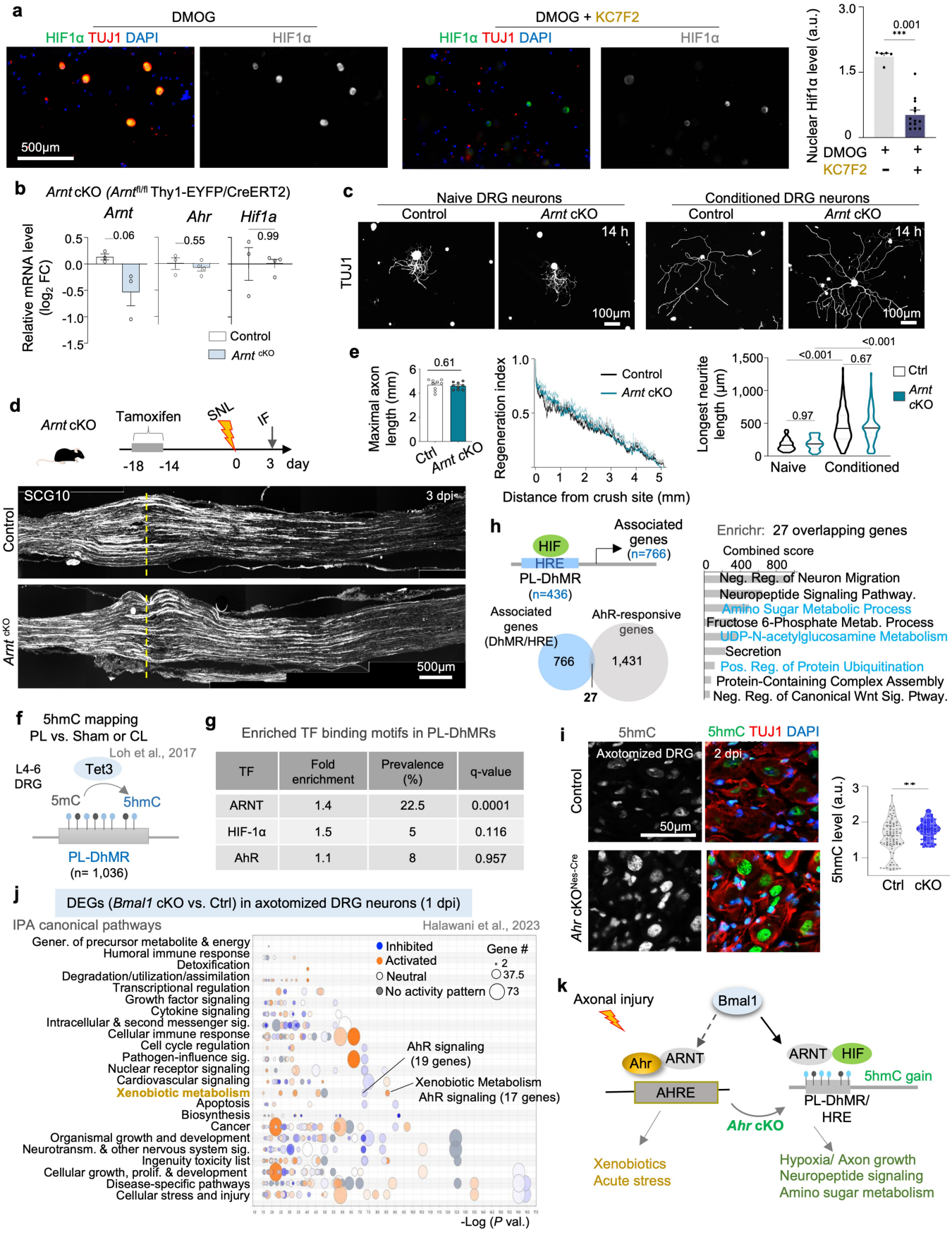

Extended Data Fig. 9 | See next page for caption.

Extended Data Fig. 9 | Neuronal *Arnt* deletion does not impair axon regeneration after sciatic nerve injury, and interaction of AhR, Bmal1, and DNA hydroxymethylation following axotomy. a, IF of DRG neurons treated with HIF stabilizer DMOG (500 μM) and with or without KC7F2 exposure (80 μM) for 12 h. n = 5 cells for DMOG and 13 for DMOG + KC7F2. Unpaired two-tailed *t*-test. **b**, qRT-PCR of DRGs from *Arnt* cKO and littermate controls. n = 3–4 /genotype (8 DRGs pooled from 2 mice/sample). Unpaired two-tailed *t*-test. **c**, IF for $TUJ1^+$ DRG neurons from naive or conditioned DRGs of *Arnt* cKO and control mice at 14 h post-seeding. Violin plots show median and quartiles from n = 51–52 naive, and 122–157 conditioned neurons from 5 mice/ genotype. Two-way ANOVA with Bonferroni correction. **d, e**, IF data of sciatic nerve crush paradigm at 14 d after tamoxifen injection (100 mg/kg i.p. x 5 d) shows comparable axon regeneration ($SCG10^+$) in *Arnt* cKO and control mice at 3 dpi. Dashed lines indicate lesion centre. n = 9 mice/genotype. Regeneration index: two-way ANOVA. Maximal axon length: unpaired two-tailed *t*-test. **f**, Genome-wide mapping of 5hmC after PL in DRGs identified 1,036 differentially hydroxymethylated regions (DhMRs) compared to sham or central lesion (CL); DhMR regulated by Tet3. **g**, Summary of HOMER motif analysis of PL-DhMRs, with fold enrichment, prevalence, and FDR (q-value) for ARNT, HIF1α, and AhR motifs. **h**, Gene transcription mediated by PL-DhMRs containing HIF response elements (HREs). Venn diagram shows 27 overlapping genes between PL-DhMR/HRE-associated genes (n = 766) and AhR-responsive PL-DEGs. Enrichr analysis of 27 shared genes. **i**, IF and quantification for 5hmC in DRGs from *Ahr* cKO (Nestin-Cre) and controls at 2 dpi after PL. n = 9 DRGs from 3 mice/genotype. Median indicated by horizontal line. Mann-Whitney two-tailed test. **j**, Bubble plot of canonical pathways enriched after *Bmal1* cKO in DRG after axotomy, with xenobiotic metabolism and AhR signalling highlighted. **k**, Working model of AhR-HIF competition for heterodimerization partner Arnt. Arnt-HIF1α complex may act at 5hmC-modified loci to regulate pro-regenerative programs in DRG neurons after axotomy. *Ahr* deletion skews Arnt activity toward the HIF1α regulon, partly gated by Bmal1-dependent 5hmC modifications. Data are mean ± s.e.m.

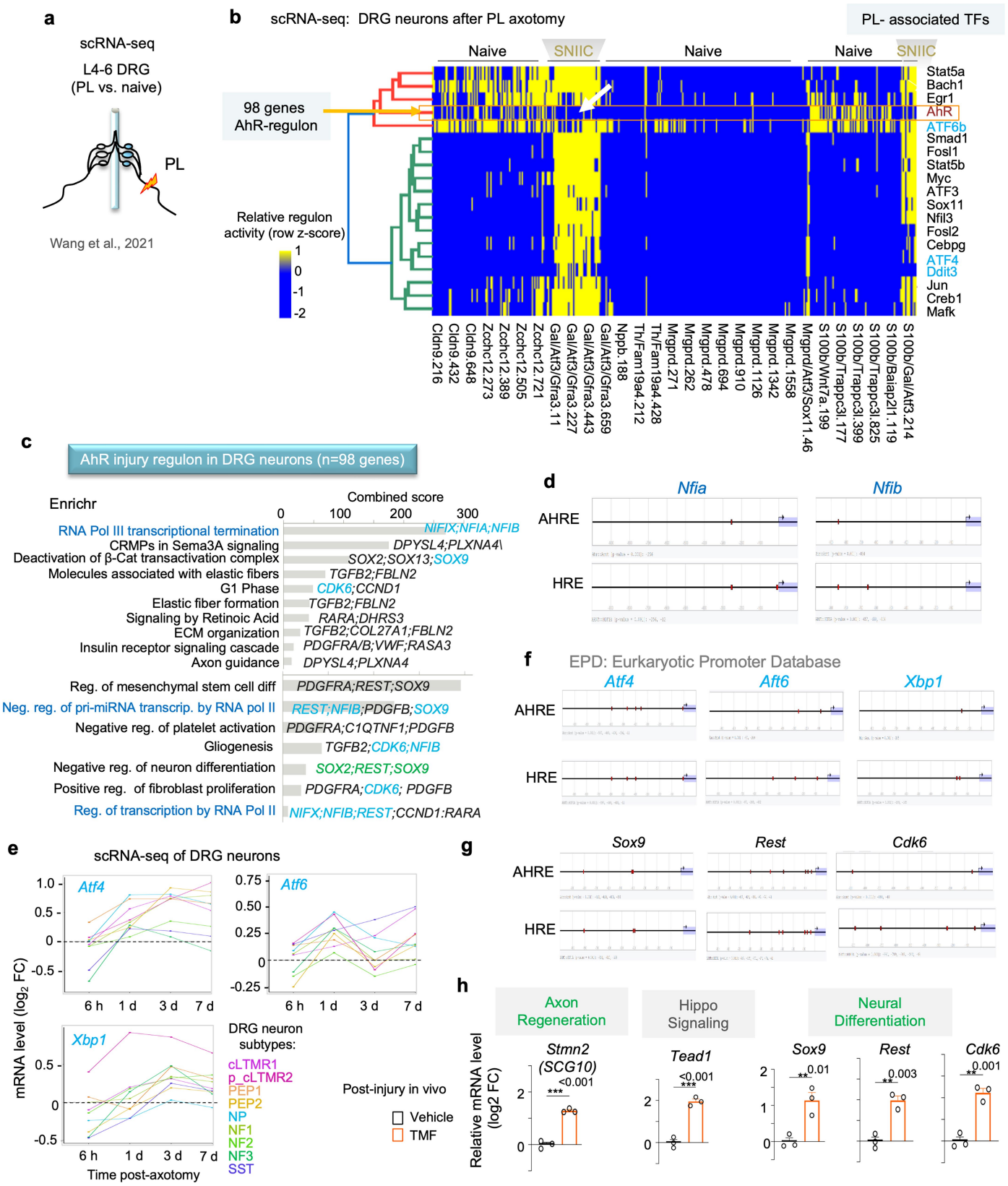

Extended Data Fig. 10 | See next page for caption.

Extended Data Fig. 10 | scRNA-seq of DRG reveals neuronal AhR injury regulon associated with RNA regulation and integrated stress response. **a**, Schematic of scRNA-seq of axotomized sciatic DRGs after PL compared to naive DRG (Wang et al.[37]). **b**, Heatmap of regulon activity scores for PL-associated transcription factors in DRG neurons after axotomy. Sciatic nerve injury-induced neuronal clusters (SNIIC), defined by ATF3 expression, showed AhR in OFF state (white arrow), in contrast to ON state for majority of TFs, including ATF3. Integrated stress response (ISR) denoted in blue. **c**, Enrichr pathway analysis of a predicted AhR regulon of 98 genes in axotomized DRG neurons, showing enrichment in RNA processing and ISR-related pathways (blue font). **d**, Eukaryotic Promoter Database analyses of AHRE and HRE motifs in promoters of *Nfia* and *Nfib* genes. **e**, scRNA-seq survey of conditioned DRG (dataset Renthal et al., 2019) shows induction of *Atf4, Atf6*, and *Xbp1* in the majority of DRG neurons after PL. **f, g**, Eukaryotic Promoter Database analyses of AHRE or HRE motifs in gene promoters. **h**, qRT-PCR analysis of genes linked to neural differentiation and axonogenesis. *Hprt1* expression was used for normalization. n = 3 independent samples (each pooled from L4-L6 DRGs from 3 mice per group). Mean ± s.e.m. Unpaired two-tailed *t*-test.

nature portfolio

Corresponding author(s): Hongyan Zou

Last updated by author(s): 2/4/2026

Reporting Summary

Nature Portfolio wishes to improve the reproducibility of the work that we publish. This form provides structure for consistency and transparency in reporting. For further information on Nature Portfolio policies, see our Editorial Policies and the Editorial Policy Checklist.

Statistics

For all statistical analyses, confirm that the following items are present in the figure legend, table legend, main text, or Methods section.

n/a	Confirmed
☐	☒ The exact sample size (*n*) for each experimental group/condition, given as a discrete number and unit of measurement
☐	☒ A statement on whether measurements were taken from distinct samples or whether the same sample was measured repeatedly
☐	☒ The statistical test(s) used AND whether they are one- or two-sided *Only common tests should be described solely by name; describe more complex techniques in the Methods section.*
☒	☐ A description of all covariates tested
☐	☒ A description of any assumptions or corrections, such as tests of normality and adjustment for multiple comparisons
☐	☒ A full description of the statistical parameters including central tendency (e.g. means) or other basic estimates (e.g. regression coefficient) AND variation (e.g. standard deviation) or associated estimates of uncertainty (e.g. confidence intervals)
☐	☒ For null hypothesis testing, the test statistic (e.g. *F*, *t*, *r*) with confidence intervals, effect sizes, degrees of freedom and *P* value noted *Give P values as exact values whenever suitable.*
☒	☐ For Bayesian analysis, information on the choice of priors and Markov chain Monte Carlo settings
☒	☐ For hierarchical and complex designs, identification of the appropriate level for tests and full reporting of outcomes
☒	☐ Estimates of effect sizes (e.g. Cohen's *d*, Pearson's *r*), indicating how they were calculated

Our web collection on statistics for biologists contains articles on many of the points above.

Software and code

Policy information about availability of computer code

Data collection	Equipment used. Fluorescence microscopy images were acquired using the Zeiss AxioVision Rel. 4.8 system equipped with Axio. Western blotting was performed using the LI-COR Odyssey Classic imaging system. Quantitative RT–PCR was conducted on an ABI Prism 7900HT Sequence Detection System. RNA sequencing was performed on the Illumina NovaSeq platform. High-content confocal imaging was carried out using the ImageXpress Micro Confocal (IXM) High-Content Imaging System (Molecular Devices, San Jose, CA).
Data analysis	Software used. GraphPad Prism v9/10 and Origin 2019/2020b were used for data visualization and statistical analysis. Image quantification was performed using Fiji/ImageJ (version 2.3.0/1.53q). Microscopy image acquisition was performed using Zeiss AxioVision Rel. 4.8, ZEN 3.6 (Blue edition), and ZEN 2012 software. Figure assembly was carried out using Microsoft PowerPoint for Microsoft 365 MSO (Version 2601, Build 16.0.19628.20132), Microsoft Paint (version 11.2511.291.0), and Adobe Photoshop CC 2019. Data handling and organization were performed using Microsoft Excel for Microsoft 365 MSO (Version 2601, Build 16.0.19628.20132). Pathway and network analyses were conducted using Ingenuity Pathway Analysis (IPA; version 153384343), STRING database, and GREAT (version 4.0; http://great.stanford.edu/public/html/index.php). Promoter analyses were performed using the Eukaryotic Promoter Database (EPD; https://epd.epfl.ch/index.php). Western blot images were acquired and processed using Image Studio Light (version 5.2.5). Quantitative RT–PCR data were analyzed using SDS software (version 2.4). High-content imaging data were analyzed using MetaXpress® software (version 6; Molecular Devices). NGS data processing was performed using the NGS-Data-Charmer pipeline, Trim Galore! (version 0.6.5), Bowtie2 (version 2.4.1), and SAMtools (version 1.10).

For manuscripts utilizing custom algorithms or software that are central to the research but not yet described in published literature, software must be made available to editors and reviewers. We strongly encourage code deposition in a community repository (e.g. GitHub). See the Nature Portfolio guidelines for submitting code & software for further information.

Data

Policy information about availability of data

All manuscripts must include a data availability statement. This statement should provide the following information, where applicable:

- Accession codes, unique identifiers, or web links for publicly available datasets
- A description of any restrictions on data availability
- For clinical datasets or third party data, please ensure that the statement adheres to our policy

Data availability
RNA-seq data generated in this study (Ahr cKO dataset) have been deposited in the NCBI Gene Expression Omnibus (GEO) under accession number GSE307639 (mm10 mouse genome assembly) and are available at: https://www.ncbi.nlm.nih.gov/geo/query/acc.cgi?acc=GSE307639. Source data underlying the figures are provided with this paper. Publicly available resources used for analysis include the STRING database (https://string-db.org), GREAT v4.0 (http://great.stanford.edu/public/html/index.php), the Eukaryotic Promoter Database (EPD; https://epd.epfl.ch/index.php), the conditioned DRG neuron single-cell RNA-seq database PainSeq (https://painseq.shinyapps.io/publish/), and the Mouse Brain Atlas for nervous system expression analysis of Ahr (http://mousebrain.org). Ingenuity Pathway Analysis (IPA; QIAGEN) was accessed under an institutional license held by the Icahn School of Medicine at Mount Sinai.

Code availability
RNA-seq analyses were performed using established and widely adopted R workflows and publicly available bioinformatics tools as stated in methods section. Additional details are available from the corresponding author upon reasonable request.

Research involving human participants, their data, or biological material

Policy information about studies with human participants or human data. See also policy information about sex, gender (identity/presentation), and sexual orientation and race, ethnicity and racism.

Reporting on sex and gender	*Use the terms sex (biological attribute) and gender (shaped by social and cultural circumstances) carefully in order to avoid confusing both terms. Indicate if findings apply to only one sex or gender; describe whether sex and gender were considered in study design; whether sex and/or gender was determined based on self-reporting or assigned and methods used. Provide in the source data disaggregated sex and gender data, where this information has been collected, and if consent has been obtained for sharing of individual-level data; provide overall numbers in this Reporting Summary. Please state if this information has not been collected. Report sex- and gender-based analyses where performed, justify reasons for lack of sex- and gender-based analysis.*
Reporting on race, ethnicity, or other socially relevant groupings	*Please specify the socially constructed or socially relevant categorization variable(s) used in your manuscript and explain why they were used. Please note that such variables should not be used as proxies for other socially constructed/relevant variables (for example, race or ethnicity should not be used as a proxy for socioeconomic status). Provide clear definitions of the relevant terms used, how they were provided (by the participants/respondents, the researchers, or third parties), and the method(s) used to classify people into the different categories (e.g. self-report, census or administrative data, social media data, etc.) Please provide details about how you controlled for confounding variables in your analyses.*
Population characteristics	*Describe the covariate-relevant population characteristics of the human research participants (e.g. age, genotypic information, past and current diagnosis and treatment categories). If you filled out the behavioural & social sciences study design questions and have nothing to add here, write "See above."*
Recruitment	*Describe how participants were recruited. Outline any potential self-selection bias or other biases that may be present and how these are likely to impact results.*
Ethics oversight	*Identify the organization(s) that approved the study protocol.*

Note that full information on the approval of the study protocol must also be provided in the manuscript.

Field-specific reporting

Please select the one below that is the best fit for your research. If you are not sure, read the appropriate sections before making your selection.

☒ Life sciences ☐ Behavioural & social sciences ☐ Ecological, evolutionary & environmental sciences

For a reference copy of the document with all sections, see nature.com/documents/nr-reporting-summary-flat.pdf

Life sciences study design

All studies must disclose on these points even when the disclosure is negative.

Sample size	The number of mice, DRGs, and cells used for all experiments is indicated clearly in the figure legends and was determined based on previous experience and consistent with publications from our group and other labs the field (please see references below).

DOI: https://doi.org/10.1523/JNEUROSCI.5397-08.2009
DOI: 10.1073/pnas.1100426108
DOI: 10.1016/j.neuron.2015.09.050
DOI: 10.1016/j.neuron.2017.03.034
DOI: 10.1523/JNEUROSCI.0589-13.2013
DOI: 10.1523/JNEUROSCI.17-02-00646.1997
DOI: 10.21769/BioProtoc.1694
In vivo analysis of nerve regeneration utilized at least 5 to 9 mice per group. In vitro DRG neuron culture and qRT-PCR analysis utilized the indicated number of DRGs obtained from a minimum of 3 mice per group unless otherwise indicted. Western blot analysis was repeated on 3 independent biological samples per time point. siRNA treatment of DRG neurons and qRT-PCR analysis were performed on 3 to 4 independent cultures. Drug treatment of induced cortical neurons was performed on 3 independently derived cultures unless otherwise indicated.

Data exclusions

No data were excluded from the analysis.

Replication

For all in vivo studies, individual animals were used as replicates. Experiments were repeated a minimum of 3 times in different mice with the exact number of mice detailed in the figure legends. In vitro experiments were replicated a minimum of 3 times.

Randomization

For all experimental groups, group allocation was randomized by age and sex. Littermates were assigned as controls and sex matched when possible. For in vitro experiments using primary neuronal cultures, allocation to experimental groups was defined by genotype or experimental treatment. Independent biological replicates were obtained from separate mice or independent dissections (typically n ≥ 3 per condition). Where applicable, neurons from a single preparation were split across treatment conditions and processed in parallel to minimize culture batch effects. Experimental conditions were standardized across groups, including plating density, culture duration, media composition, and processing workflows. Multiple technical replicates (e.g., wells or coverslips) were analyzed for each biological replicate. Quantification was performed using consistent analysis pipelines under identical acquisition and processing parameters. The number of independent biological replicates (independent cultures or mice) and technical replicates analyzed for each experiment is specified in the corresponding legends of each figure.

Blinding

Blinding during data collection was not always feasible because experimental group identity (e.g., genotype or treatment condition) was inherent to sample preparation, culture handling, or imaging workflows (ie. cKO mice expressed EYFP, while controls didn't). To minimize bias, experimental conditions were processed in parallel using standardized acquisition parameters and objective quantitative readouts. Data analyses were performed in a blinded manner wherever possible, frequently involving independent quantification by two investigators. The experiments in which blinded analysis was conducted are specified below; for experiments where blinding was not practical, analyses relied on standardized quantification pipelines to reduce potential observer bias. Analysis for Fig. 3e was conducted under blinded conditions. Experiments underlying Fig. 2i, Extended Data Fig. 2i, Extended Data Fig. 3d, Extended Data Fig. 3f, Extended Data Fig. 5a, Fig. 5d, and Fig. 5e were not blinded for the reasons outlined above.

Reporting for specific materials, systems and methods

We require information from authors about some types of materials, experimental systems and methods used in many studies. Here, indicate whether each material, system or method listed is relevant to your study. If you are not sure if a list item applies to your research, read the appropriate section before selecting a response.

Materials & experimental systems

n/a	Involved in the study
☐	☒ Antibodies
☐	☒ Eukaryotic cell lines
☒	☐ Palaeontology and archaeology
☐	☒ Animals and other organisms
☒	☐ Clinical data
☒	☐ Dual use research of concern
☒	☐ Plants

Methods

n/a	Involved in the study
☒	☐ ChIP-seq
☒	☐ Flow cytometry
☒	☐ MRI-based neuroimaging

Antibodies

Antibodies used

Primary antibodies used were as follows:
anti-AHR (rabbit, 1:300, Enzo BML-SA210, RRID:AB_10540536),
anti-CYP1B1 (rabbit, 1:1000, Invitrogen PA5-95277, RRID:AB_2807081)
anti-ATF3 (rabbit, 1:300, Santa Cruz sc-188, RRID:AB_2258513),
anti-Tubulin β3 (TUJ1, mouse, 1:1,000, Biolegend 801201, RRID:AB_2313773),
anti-Tubulin β3 (D71G9, rabbit, 1:300, Cell Signaling 5568S, RRID:AB_10694505),
anti-SCG10/STMN2 (rabbit, 1:1,000, Novus NBP1-49461, RRID:AB_10011569),
anti-GFP (chicken, 1:1,000, Aves Lab GFP-1020, RRID:AB_10000240),
anti-IBA1 (rabbit, 1:1,000, Wako 019-19741, RRID:AB_839504),
anti-pS6 ribosomal protein-S235/236 (rabbit, 1:300, Cell Signaling 2211, RRID:AB_331679),
anti-5hmC (rabbit, 1:500, Active Motif 39769, RRID:AB_10013602),
anti-CD8a (rat, 1:100, Invitrogen 14-0081-82, RRID:AB_467087),
anti-CD4 (rat, 1:100, Invitrogen 14-0041-82, RRID:AB_467063),
anti-CD68 (rat, 1:100, Biolegend 137002, RRID:AB_2044004),
anti-CD45 (rat, 1:100, BD Pharmingen 550539, RRID:AB_2174426),

anti-PU1 (E.388.3) (rabbit, 1:300, Thermofisher MA5-15064, RRID:AB_10986949),
anti-F4/80 (rat, 1:300, Thermofisher 14-4801-81, RRID:AB_467557),
anti-CD206 (goat, 1:200, R&D systems AF2535, RRID:AB_2063012),
anti-Sox10 (goat, 1:50, R&D systems AF2864, RRID:AB_442208),
anti-PGP9.5 (rabbit, 1:800, Neuromics, RA12103, RRID:AB_2315126),
anti-NFH (chicken, EMD Millipore AB5539, 1:1,000, RRID:AB_11212161),
anti- CSPG (CS-56) (mouse, Sigma C8035, 1:100, RRID:AB_476879),
anti-GFAP (chicken, Aves Labs GFAP, 1:500, RRID:AB_2858088),
anti-puromycin (mouse, DSHB, PMY-2A4, 1:100, RRID:AB_2619605),
anti-phospho-Eif2a (S51) (D9G8)(rabbit, Cell Signaling, 3398, 1:300, RRID:AB_2096481),
anti-E-Cadherin (24E10) (rabbit, Cell Signaling 3195, 1:300, RRID:AB_2291471),
anti-Ly6G (rat, Biolegend 127601, 1:100, RRID:AB_1089179),
anti-Hif1a (rabbit, Novus NB100-479, 1:300, RRID:AB_10000633),
anti-CGRP (rabbit, Cell Signal #14959, 1:300, RRID:AB_2798662),
anti-β-Actin (mouse, 1:10,000, Sigma A1978, RRID:AB_476692).

The following Alexa-conjugated donkey secondary antibodies (Jackson ImmunoResearch) were used at 1:300 dilution of a 1 mg/ml stock solution (in 50% glycerol).
AlexaFluor 488 anti-rabbit IgG (711-545-152),
AlexaFluor 488 anti-chicken IgY (703-545-155),
AlexaFluor 594 anti-rabbit IgG (711-585-152),
AlexaFluor 594 anti-mouse IgG (711-585-150),
AlexaFluor 594 anti-rat IgG (712-585-153),
AlexaFluor 647 anti-rabbit IgG (711-605-152),
AlexaFluor 647 anti-mouse IgG (715-605-151).

Validation

Antibody validation. All primary antibodies were selected based on manufacturer validation for the indicated species and applications. Validation documentation, including specificity testing, expected molecular weight or localization patterns, and application suitability, is available on the respective manufacturer product webpages listed below. RRID identifiers are provided for all antibodies to ensure unambiguous resource identification.

Primary antibodies used were as follows: anti-AHR (rabbit, 1:300, Enzo Life Sciences BML-SA210; RRID:AB_10540536; https://www.enzolifesciences.com/BML-SA210/aryl-hydrocarbon-receptor-polyclonal-antibody/); anti-CYP1B1 (rabbit, 1:1000, Invitrogen PA5-95277; RRID:AB_2807081; https://www.thermofisher.com/antibody/product/CYP1B1-Antibody-Polyclonal/PA5-95277); anti-ATF3 (rabbit, 1:300, Santa Cruz sc-188; RRID:AB_2258513; https://datasheets.scbt.com/sc-188.pdf); anti-β3-tubulin/TUJ1 (mouse, 1:1000, BioLegend 801201; RRID:AB_2313773; https://www.biolegend.com/ja-jp/products/purified-anti-tubulin-beta-3-tubb3-antibody-11580?GroupID=GROUP686); anti-β3-tubulin (rabbit, 1:300, Cell Signaling Technology 5568S; RRID:AB_10694505; https://www.cellsignal.com/products/primary-antibodies/b3-tubulin-d71g9-xp-rabbit-mab/5568); anti-SCG10/STMN2 (rabbit, 1:1000, Novus NBP1-49461; RRID:AB_10011569; https://www.novusbio.com/products/stathmin-2-stmn2-antibody_nbp1-49461); anti-GFP (chicken, 1:1000, Aves Labs GFP-1020; RRID:AB_10000240; https://www.aveslabs.com/products/anti-green-fluorescent-protein-antibody-gfp); anti-IBA1 (rabbit, 1:1000, Wako 019-19741; RRID:AB_839504; https://labchem-wako.fujifilm.com/us/product/detail/W01W0101-1974.html); anti-phospho-S6 (Ser235/236) (rabbit, 1:300, Cell Signaling Technology 2211; RRID:AB_331679; https://www.cellsignal.com/products/primary-antibodies/phospho-s6-ribosomal-protein-ser235-236-antibody/2211); anti-5hmC (rabbit, 1:500, Active Motif 39769; RRID:AB_10013602; https://www.activemotif.com/catalog/details/39769/5-hydroxymethylcytidine-5-hmc-antibody); anti-CD8a (rat, 1:100, Invitrogen 14-0081-82; RRID:AB_467087; https://www.thermofisher.com/antibody/product/CD8a-Antibody-clone-53-6-7-Monoclonal/14-0081-82); anti-CD4 (rat, 1:100, Invitrogen 14-0041-82; RRID:AB_467063; https://www.thermofisher.com/antibody/product/CD4-Antibody-clone-GK1-5-Monoclonal/14-0041-82); anti-CD68 (rat, 1:100, BioLegend 137002; RRID:AB_2044004; https://www.biolegend.com/de-de/products/purified-anti-mouse-cd68-antibody-6421?GroupID=BLG8725); anti-CD45 (rat, 1:50, BD Biosciences 550539; RRID:AB_2174426; https://www.bdbiosciences.com/en-us/products/reagents/microscopy-imaging-reagents/immunohistochemistry-reagents/purified-rat-anti-mouse-cd45.550539); anti-PU.1 (rabbit, 1:300, Thermo Fisher MA5-15064; RRID:AB_10986949; https://www.thermofisher.com/antibody/product/PU-1-Antibody-clone-E-388-3-Monoclonal/MA5-15064); anti-F4/80 (rat, 1:300, Thermo Fisher 14-4801-81; RRID:AB_467557; https://www.fishersci.se/shop/products/f4-80-monoclonal-antibody-bm8-ebioscience-invitrogen/15277387); anti-CD206 (goat, 1:200, R&D Systems AF2535; RRID:AB_2063012; https://www.rndsystems.com/products/mouse-mmr-cd206-antibody_af2535); anti-SOX10 (goat, 1:50, R&D Systems AF2864; RRID:AB_442208; https://www.rndsystems.com/products/human-sox10-antibody_af2864); anti-PGP9.5 (rabbit, 1:800, Neuromics RA12103; RRID:AB_2315126; https://www.neuromics.com/RA12103); anti-NFH (chicken, 1:1000, Millipore AB5539; RRID:AB_11212161; https://www.sigmaaldrich.com/US/en/product/mm/ab5539); anti-CSPG (CS-56) (mouse, 1:100, Sigma C8035; RRID:AB_476879; https://www.sigmaaldrich.com/US/en/product/sigma/c8035); anti-GFAP (chicken, 1:500, Aves Labs; RRID:AB_2858088; https://www.antibodiesinc.com/products/anti-glial-fibrillary-acidic-protein-antibody-gfap); anti-puromycin (mouse, 1:100, DSHB PMY-2A4; RRID:AB_2619605; https://dshb.biology.uiowa.edu/PMY-2A4); anti-phospho-eIF2α (Ser51) (rabbit, 1:300, Cell Signaling Technology 3398; RRID:AB_2096481; https://www.cellsignal.com/products/primary-antibodies/phospho-eif2a-ser51-d9g8-xp-rabbit-mab/3398); anti-E-cadherin (rabbit, 1:300, Cell Signaling Technology 3195; RRID:AB_2291471; https://www.cellsignal.com/products/primary-antibodies/e-cadherin-24e10-rabbit-mab/3195); anti-Ly6G (rat, 1:100, BioLegend 127601; RRID:AB_1089179; https://www.biolegend.com/en-gb/products/purified-anti-mouse-ly-6g-antibody-4767); anti-HIF-1α (rabbit, 1:300, Novus NB100-479; RRID:AB_10000633; https://www.novusbio.com/primary-antibodies/hif-1-alpha); anti-CGRP (rabbit, 1:300, Cell Signaling Technology 14959; RRID:AB_2798662; https://www.cellsignal.com/products/primary-antibodies/cgrp-d5r8f-rabbit-monoclonal-antibody/14959).

Eukaryotic cell lines

Policy information about cell lines and Sex and Gender in Research

Cell line source(s)	The H9 human embryonic stem cell line (Cat#: WA09) was acquired from WiCell via the Mount Sinai Stem Cell Core Facility, under an existing Material Transfer Agreement (MTA) held by the core facility (contact info:samuele.marro@mssm.edu).
Authentication	Cell-lines were obtained directly from source and were not further validated in the lab.
Mycoplasma contamination	Cell lines was tested negative for mycoplasma contamination by using IDEXX RADIL service.
Commonly misidentified lines (See ICLAC register)	No commonly misidentified cell lines were used in this work.

Animals and other research organisms

Policy information about studies involving animals; ARRIVE guidelines recommended for reporting animal research, and Sex and Gender in Research

Laboratory animals	Mouse strains were obtained from The Jackson Laboratory (C57BL/6J, RRID:IMSR_JAX:000664; Tg(Thy1-cre/ERT2,-EYFP)HGfng, also known as SLICK-H, RRID:IMSR_JAX:012708; B6.Cg-Tg(Nes-cre)1Kln/J, RRID:IMSR_JAX:003771; Ahr^fl/fl, RRID:IMSR_JAX:006203). Arnt^fl/fl mice were provided by Dr. Frank Gonzalez (NIH). Animal procedures were conducted under an approved protocol (IPROTO202200000184) from the Institutional Animal Care and Use Committee (IACUC) at Mount Sinai. All mice were maintained on a C57BL/6J genetic background for at least three generations. Animals were housed in a specific pathogen-free barrier facility under a 12-h light/dark cycle with ad libitum access to food and water. Ambient temperature was maintained at approximately 18–23 °C with relative humidity of 40–60%. Mice were group-housed (up to five per cage) in corn bedding-lined cages with standard pellet chow and water bottles and were acclimated to the facility for at least two weeks prior to experimentation. All mice used in the study were young adults (<30 weeks of age), unless otherwise indicated.
Wild animals	The study did not involve wild animals.
Reporting on sex	We used mixed sex for all experiments.
Field-collected samples	This study does not involve field work.
Ethics oversight	All animal procedures complied with ethical regulations for animal testing and research and were performed according to protocols approved by the Institutional Animal Care and Use Committee (IACUC) at Icahn School of Medicine at Mount Sinai (approved protocol# IPROTO202200000184). H9 human embryonic stem (hES) cells studies were approved by the Embryonic Stem Cell Research Oversight Committee (ESCRO) at Icahn School of Medicine at Mount Sinai.

Note that full information on the approval of the study protocol must also be provided in the manuscript.

Plants

Seed stocks	*Report on the source of all seed stocks or other plant material used. If applicable, state the seed stock centre and catalogue number. If plant specimens were collected from the field, describe the collection location, date and sampling procedures.*
Novel plant genotypes	*Describe the methods by which all novel plant genotypes were produced. This includes those generated by transgenic approaches, gene editing, chemical/radiation-based mutagenesis and hybridization. For transgenic lines, describe the transformation method, the number of independent lines analyzed and the generation upon which experiments were performed. For gene-edited lines, describe the editor used, the endogenous sequence targeted for editing, the targeting guide RNA sequence (if applicable) and how the editor was applied.*
Authentication	*Describe any authentication procedures for each seed stock used or novel genotype generated. Describe any experiments used to assess the effect of a mutation and, where applicable, how potential secondary effects (e.g. second site T-DNA insertions, mosiacism, off-target gene editing) were examined.*